

A mechanism for the generation of robust circadian oscillations through ultrasensitivity and differential binding affinity

Agnish Kumar Behera and Clara del Junco and Suriyanarayanan Vaikuntanathan
Department of Chemistry and The James Franck Institute, University of Chicago, Chicago, IL, 60637

Biochemical circadian rhythm oscillations play an important role in many signalling mechanisms. In this work, we explore some of the biophysical mechanisms responsible for sustaining robust oscillations by constructing a minimal but analytically tractable model of the circadian oscillations in the KaiABC protein system found in the cyanobacteria *S. elongatus*. In particular, our minimal model explicitly accounts for two experimentally characterized biophysical features of the KaiABC protein system, namely, a differential binding affinity and an ultrasensitive response. Our analytical work shows how these mechanisms might be crucial for promoting robust oscillations even in sub optimal nutrient conditions. Our analytical and numerical work also identifies mechanisms by which biological clocks can stably maintain a constant time period under a variety of nutrient conditions. Finally, our work also explores the thermodynamic costs associated with the generation of robust sustained oscillations and shows that the net rate of entropy production alone might not be a good figure of merit to assess the quality of oscillations.

I. INTRODUCTION

Most living organisms, ranging from simple single celled organisms like cyanobacteria to multicellular organisms possess an internal clock which is entrained with the day-night cycle [1–5]. The fidelity and robustness of this clock is crucial for the well being and survival of the organism [6–9]. The time period of the internal clock has, for example, been found to be robust with respect to changes in the temperature, nutrient conditions, and pH [10–13]. Understanding the biochemical and thermodynamic underpinnings of such robust behavior remains an important challenge given the crucial biological role of the internal clock.

The KaiABC protein system (see Fig. 1) provides a minimal biochemically tractable model to explore the above mentioned questions. The KaiABC system is found in cyanobacteria *S. elongatus* where it plays the role of regulating the circadian cycle. The KaiABC system consists of three proteins, KaiA, KaiB and KaiC [14]. In vitro, the system of KaiABC proteins undergoes sustained oscillations as evidenced by the phosphorylation state of the KaiC protein. These oscillations have been shown to have many of the same robust features as those observed in the circadian oscillations they support in cyanobacteria [15, 16]. The KaiABC model system has been probed in many experimental and theoretical studies [10, 14]. These have elucidated some of the necessary requirements for the generation of sustained oscillations [10, 15, 17–21]. Despite these advances, understanding the biochemical and biophysical driving forces that are responsible for sustaining robust oscillations remains an open question [10, 14, 16, 19, 21, 22].

In this paper, we build on recent experimental and modelling work in Ref [17] and show how a particular ultrasensitive switch in the KaiABC biochemical circuit can control the quality and robustness of oscillations. In particular, in Ref [17], the authors identify a previously underappreciated ultrasensitive response in the phospho-

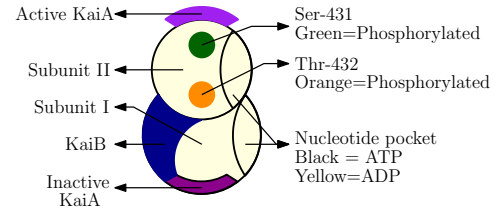


FIG. 1: KaiC monomer. The KaiC protein exists as a hexamer and each monomer consists of 2 domains, CI and CII. The CII domain has two phosphorylation sites, Ser-431 and Thr-432, a KaiA binding site and a nucleotide binding site (which binds either ATP or ADP). The CI domain binds to KaiB and helps sequester KaiA. Subsequently, the KaiABC complex will be denoted using $-/A/B CI_{TP/DP} -/A CII_{TP/DP}^{U/T/S/D}$. Here TP/DP denotes ATP/ADP attached to the domain. U denotes none of the sites in CII are phosphorylated, S means only Serine site is phosphorylated, T means Threonine site is phosphorylated, D denotes doubly phosphorylated form. A attached to CI denotes sequestered KaiA, A attached to CII denotes active KaiA acting as an assistant in phosphorylation. B attached to CI implies inactive form which will start sequestering KaiA.

rylation levels of the KaiC proteins as the concentration of the KaiA proteins is tuned. The KaiB proteins play no role in this ultrasensitive response. It was postulated in Ref [17] that this ultrasensitive switch plays a central role in ensuring robust oscillations. Specifically, the ultrasensitive switch allows the system to exhibit sustained oscillations even at low levels of the energy rich molecule, ATP [17]. Motivated by this work, we build a minimal Markov state model that provides analytical insight for how an ultrasensitive KaiA-KaiC switch can modulate the quality of oscillations. Our minimal model also allows us to analytically study how another biophysical driving force, namely the differential affinity of the different forms of KaiC to KaiA [10, 15, 19, 22] also control oscillations. Finally, our minimal Markov state model

allows us to comment on the thermodynamic costs associated with setting up robust oscillations in the KaiABC system.

The rest of the paper is organized as follows. We first briefly review the salient features of the KaiABC biochemical circuit and then outline our minimal model. This model captures the above mentioned features of the KaiABC circuit, namely the differential affinity of KaiC to KaiA binding, and the ultrasensitive response of KaiC phosphorylation levels to changes in KaiA concentration. It also additionally accounts for many other experimentally characterized biophysical forces [14]. We then write down a stochastic master equation to describe the dynamics of our model. This stochastic master equation is non-linear in the probability. The non-linearity is due to the various feedback mechanisms that are necessary for sustaining oscillations. Interestingly, by solving the non-linear stochastic master equation, we are able to an-

alytically describe the emergence of global oscillations in response to changing the differential affinity [21]. Our model allows us to obtain approximate analytical solutions that provide qualitative insight into how tuning ultrasensitivity tunes the quality of oscillations. Crucially, our results allow us to elucidate how an ultrasensitive switch can support oscillations even at a lower concentration of ATP. Our results also allow us to explain how the time period of oscillations can be robustly maintained even as the concentration of ATP is tuned, a phenomenon known as affinity compensation. Finally, we comment on the thermodynamic costs associated with sustaining robust oscillations.

II. KAIABC OSCILLATOR AND MODEL DETAILS

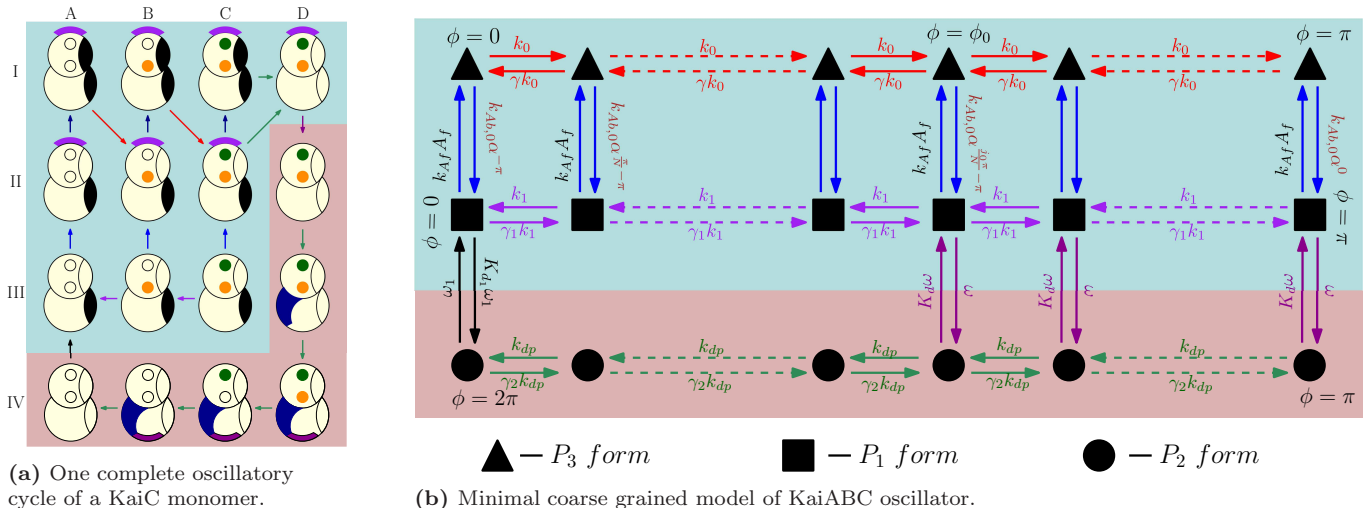


FIG. 2: In Fig. 2a, rows are labelled by I, II, III, IV and columns are labelled by A, B, C, D. In Fig. 2a, the color in the reaction arrows correspond to those in Fig. 2b. Active conformations are denoted using a cyan background and inactive conformations are denoted using a red background. In our model (Fig. 2b), the horizontal axis represents the amount of phosphorylation in the system, with $\phi = 0$ and $\phi = 2\pi$ corresponding to the completely dephosphorylated state and $\phi = \pi$ corresponding to the completely phosphorylated hexamer. The phosphorylation function is a linearly increasing function, 0 at $\phi = 0$, 1 at $\phi = \pi$ and then symmetrically decreasing from $\phi = \pi$ to 2π . Thus, phosphorylation, $\mathcal{P} = \sum_{\phi} \frac{\phi}{\pi} (P_1(\phi) + P_3(\phi)) + \sum_{\phi} (2 - \frac{\phi}{\pi}) P_2(\phi)$. Changes in the phosphorylation levels of the KaiC hexamers give rise to oscillations. KaiA binds to KaiC during the "day" and promotes phosphorylation, whereas at "night", KaiB binds to KaiC and sequesters KaiA thus leading to dephosphorylation. The horizontal rungs in all the states, correspond to the phosphotransfer reactions and the hydrolysis of ATP accompanying it, i.e. the red arrows between $IA \rightarrow IIB$, $IB \rightarrow IIC$, purple arrows between $IIIC \rightarrow IIIA$, green arrows between $IVD \rightarrow IVA$ in Fig. 2a. The ratio of the forward and backward rates is given by, $\gamma, \gamma_1, \gamma_2$ which are all less than 1, because of the fact that these describe reactions coupled to ATP hydrolysis which are inherently irreversible. In the model, $\alpha > 1$ is responsible for differential affinity, $K_{d0} \equiv \frac{k_{Ab,0}}{k_{Af}}$ corresponds to % ATP and k_1 helps in tuning ultrasensitivity. Free KaiA, A_f provides non linearity to the system.

The KaiC protein, complexed with KaiA, and KaiB proteins forms the core of the KaiABC oscillator system. The various possible states of the KaiC protein are

described in Fig. 1. Our minimal model, described in Fig. 2b and inspired by Ref. [21] (with additional modifications to include features such as ultrasensitivity) can

be viewed as a coarse-grained description of the various biochemical states accessed by the KaiABC protein system [14]. In the full KaiABC cycle, the KaiABC has two conformations, an active conformation (cyan background in Fig. 2) which can phosphorylate the Ser and Thr sites with KaiA as an assistant molecule and an inactive conformation (red background in Fig. 2) which sequesters KaiA with the help of KaiB and dephosphorylates the Thr and Ser sites. In our model, the P_1 and P_3 states correspond to the active conformation and P_2 to the inactive conformation.

The various biochemical states of the KaiABC protein are summarized in Fig. 1 and Fig. 2. Below, we briefly recap the various salient features of the KaiABC oscillatory cycle and explain how they are taken into account in our minimal model.

A. Differential binding of KaiA to KaiC drives the phosphorylation phase

At the beginning of the cycle, most of the KaiC is in the active conformation in $CI_{DP} - CII_{DP}^U$ form ($IIIA$ in Fig. 2a, $P_1(0)$ in Fig. 2b) and most of the KaiA is free. Depending on the phosphorylation level of active KaiC, it binds differently with KaiA. At low levels of phosphorylation ($IIIA, IIIB$) KaiC binds very strongly with KaiA. By contrast, the affinity of KaiA for KaiC is low when the KaiC is in a highly phosphorylated state ($IIIC, IIID$). This phenomena is termed as *differential affinity* of KaiC for KaiA dimers [23]. Our model captures this effect through the parameter α , where $\alpha > 1$. Specifically, the rates of $P_1 - P_3$ exchange are given by $k_{Af}A_f$ (where A_f is the free KaiA concentration) from P_1 to P_3 and by $k_{Ab,0}\alpha^{\phi-\pi}$ in the reverse direction. As phosphorylation level increases with ϕ , the term $\alpha^{\phi-\pi}$ ensures that proportion of P_1 (KaiA unbound) states increases. The extent of differential affinity in our model can be tuned by varying the parameter α . Differential affinity ensures that the unphosphorylated $IIIA$ state is primed for KaiA binding at the start of the phosphorylation cycle. Indeed, KaiA binding to the $IIIA$ state transitions the system into the IIA and IA states. Subsequently, KaiA facilitates rapid exchange of nucleotides which lead to formation of more ATP bound states and pushes the system towards phosphorylation i.e. it leads to the formation of $CI_{TP} -^A CII_{TP}^S$, $CI_{TP} -^A CII_{TP}^T$ and $CI_{TP} -^A CII_{TP}^D$ states (IB, IC and ID states respectively in the schematic).

B. Dependence of the kinetic rates on the ATP concentration

The concentration of the energy rich molecule, ATP, is an important external condition for the cyanobacteria which affect the KaiABC oscillator. It has been observed that oscillations with almost the same time

period are sustained till %ATP in the system reaches 25% below which oscillations vanish completely [10]. Here $\%ATP \equiv \frac{[ATP]}{[ATP]+[ADP]}$. In our model, the concentration of ATP controls the kinetics of the crucial $ATP - ADP$ nucleotide exchange reaction [14]. Since in our minimal model the reaction corresponding to $III(A, B, C) \rightarrow I(A, B, C)$ is coarse grained into, $P_1(i) \rightarrow P_3(i)$ and since the second step in these reactions i.e. $II(A, B, C) \rightarrow III(A, B, C)$ is dependent on %ATP, the of %ATP in our model is set by the ratio of the rates connecting the P_1 to the P_3 states,

$$K_{d0} \equiv \frac{k_{Ab,0}}{k_{Af}}. \quad (2.1)$$

Increasing K_{d0} decreases the rate of transitions to the P_3 form and thus corresponds to lower %ATP and vice versa.

C. Dynamics of the dephosphorylation phase

In the hexamer, the dephosphorylation phase starts even before total phosphorylation of each and every monomer. Specifically, once the number of serine sites phosphorylated becomes larger than the number of threonine sites which are occupied, the KaiA dissociates from the complex, the KaiC transform into an inactive conformation and the dephosphorylation phase kicks off. This transition corresponds to $ID \rightarrow IID$ in the schematic Fig. 2a and to the vertical rungs between P_1 and P_2 states colored *magenta* in our model Fig. 2b.

The dephosphorylation phase ($IVD \rightarrow IVA$) is relatively simple. It does not require KaiA as an assistant molecule for the reactions. When the proportion of doubly phosphorylated KaiC (ID, IID) is high, KaiB binding to the CI domain of KaiC is triggered, $IID \rightarrow IIID$. In our model the KaiB binding to KaiC is taken into account implicitly during the transition from P_1 to P_2 states. KaiB bound KaiC, $^B CI_{DP} - CII_{DP}^D$ ($IIID$) sequesters KaiA i.e. binds to KaiA and makes it unavailable for active use. This is taken into account through the parameter ϵ_{seq} in our model which reduces the free KaiA in the system by an amount $\epsilon_{seq} \sum P_2$. The dephosphorylation proceeds through the serine sites and then the threonine sites. Dephosphorylation reactions occur through phosphotransfer[22]. This corresponds to the system moving through the P_2 states in our model. As the reactions reach the completely dephosphorylated state $^A B CI_{DP} - CII_{DP}^U$ (IVB), the KaiABC complex starts dissociating into KaiC, KaiB and release free KaiA into the system ($IVB \rightarrow IVA$). The connection between $P_2(0)$ and $P_1(0)$ in our model taken this dissociation step. This prepares the system for the next cycle.

D. Ultrasensitive response of KaiC phosphorylation to KaiA concentration

It has been experimentally observed that in the absence of KaiB in the system, KaiC shows an ultrasensitive response in phosphorylation to KaiA concentration in the system i.e. the phosphorylation level of the KaiC hexamers change rapidly within a very narrow range of total KaiA concentration [10, 17]. This ultrasensitivity was speculated to be an important prerequisite for sustaining robust oscillations, particularly in conditions wherein the concentration of the energy rich molecule, ATP is low. Our model captures the ultrasensitive response observed in [17] and described in Section. II, through the introduction of the dephosphorylation rate k_1 (see Fig. 3). Indeed, a standard way to obtain ultrasensitive response is through the action of two antagonistic enzymes working at saturation [24, 25]. Under such conditions, the response of the system changes rapidly over a very narrow range of the enzyme concentration. In the KaiABC system the roles of the antagonistic enzymes are played by KaiA, which acts as a kinase phosphorylating KaiC and KaiC, which acts as its own phosphatase dephosphorylating itself [10, 22].

The rate k_1 in our model captures this dephosphorylation. Tuning dephosphorylation rates by increasing k_1 leads to competition between phosphorylation in the P_3 states and dephosphorylation in the P_1 states. In the absence of KaiB, which corresponds to setting $\omega = \omega_1 = 0$ in our model, we consequently observe an ultrasensitive response of phosphorylation level of KaiC to changes in the KaiA concentration (Fig. 3).

E. Dependence of the kinetic rates on the KaiA concentration

As has been described above, the rates of transition between the P_1 and P_3 states in our minimal model depend on the concentration of free KaiA, A_f . The amount of free KaiA in turn depends on the concentrations of the P_3 and P_2 states since the KaiC complex is bound to KaiA in these states. Subsequently, $A_f = A_t - (\sum_{\phi} P_3(\phi) + \epsilon_{seq} \sum_{\phi} P_2(\phi))$. As the amount of P_3 and P_2 states increase, the free KaiA concentration decrease. This step gives rise to non-linearity in the system.

III. ROLE OF DIFFERENTIAL AFFINITY AND ULTRASENSITIVITY: INSIGHTS FROM AN ANALYTICAL TREATMENT OF THE NON-LINEAR FOKKER PLANCK EQUATIONS

Our minimal model described in Fig. 2b and Sec. II can be represented mathematically using a non-linear Fokker-Planck equation, $\frac{\partial \vec{P}}{\partial t} = \mathbf{W}\vec{P}$ where \vec{P} is the probability vector of all the states (P_1, P_2, P_3) and $\mathbf{W} = \mathbf{W}(\vec{P})$ is

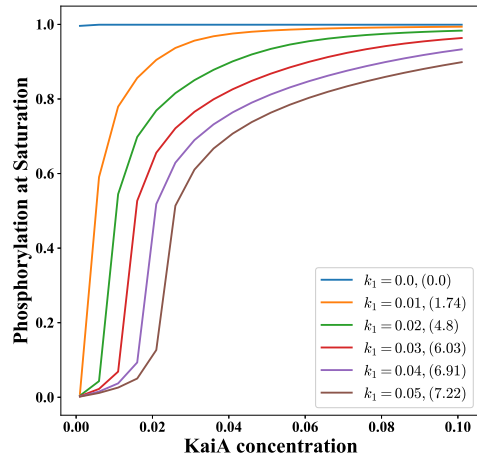


FIG. 3: Ultrasensitive response in phosphorylation of KaiC wrt the total KaiA concentration for $K_{d0} = 10$ and $\alpha = 10$. The values in the bracket are the Hill Coefficients for the response curves (calculated using the method of relative amplification [26]). Values of other parameters are given in Table. S2. These kinetics are in the absence of KaiB and P_2 states ($\omega = \omega_1 = 0$) i.e. they represent only the active form of KaiC in Fig. 2b. Thus there are no oscillations and the system always settles into a final steady state.

the rate matrix dependent on the state of the system. The non linear Fokker-Planck equation is described in full detail in S1.

If there were no nonlinearity in the Fokker-Planck equation, the Perron-Fobenius theorem would have ensured that the Fokker-Planck equation has a stable time independent steady-state solution. The oscillatory solutions of the rate-matrix decay with time as they have eigenvalues with a negative real part. Due to the non linearity in the Fokker-Planck equation in (S1.5), time dependent oscillatory steady state solutions may be possible.

In this work, we focus on how the solutions of the Fokker-Planck equation change as two specific parameters, namely, α controlling the differential affinity and k_1 controlling the ultrasensitivity are varied. In particular, we analytically show how the system can be made to transition from a time independent steady state, where it cannot function as a biological clock, to a time dependent steady state, where it can function as a biological clock, as the differential affinity parameter α is tuned. For the case where the ultrasensitivity parameter k_1 is tuned, we take inspiration from our solution from tuning α , and obtain an approximate solution. Our approximate analytical arguments provide insight into how ultrasensitivity also supports the functioning of the biological clock.

Finally, as has been reported in many experimental and theoretical studies [10, 14, 16], oscillations are affected by the concentration of %ATP in the system. In

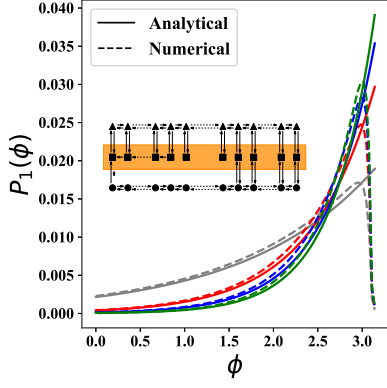


FIG. 4: Comparison between numerical and analytical results for time-independent solution of P_1 states (3.2) for different α 's. The figure in inset is a representation of the Markov State network with the P_1 states highlighted. In the main figure, *grey* corresponds to $\alpha = 2$, *red* to $\alpha = 4$, *blue* to $\alpha = 6$ and *green* to $\alpha = 8$

particular, it has been found that KaiABC system cannot sustain oscillations below a critical ATP concentration. In the next section, we will use our minimal model to show how stronger differential affinity and a better ultrasensitive switch can in fact sustain oscillations even at lower ATP concentrations [17].

We begin our analytical treatment by first considering the case where $k_1 = 0$, i.e. in a model devoid of ultrasensitivity. In this case, a time independent solution for the non-linear Fokker-Planck equation can be obtained in the limit when $\epsilon_{seq} = 0$ and $\phi_0 = \pi$. $\epsilon_{seq} = 0$ corresponds to absence of KaiA sequestration by KaiB bound KaiC states. $\phi_0 = \pi$ means that the dephosphorylation phase starts only after all the KaiC have become doubly phosphorylated. Our analytical derivation is discussed in detail in S2 A and leads to the following solutions.

$$P_3(j) = b \quad \forall j \in [0, N] \quad (3.1)$$

$$P_1(j) = \frac{1}{k_{Af}A_f} \left[k_{Ab}\alpha^{\frac{j\pi}{N}} + (\delta_{0,j} - \delta_{j_0,j})k_0(1 - \gamma) \right] b \quad \forall j \in [0, N] \quad (3.2)$$

$$P_2(2N - j) = \frac{k_0}{k_2} \left(\frac{1 - \gamma}{1 - \gamma_2} \right) b + \gamma_2^j [k_0(1 - \gamma) \left(\frac{1}{\omega_1} - \frac{1}{k_2(1 - \gamma_2)} \right) + \frac{K_D}{k_{Af}A_f} (k_0(1 - \gamma) + k_{Ab})] \quad \forall j \in [0, N] \quad (3.3)$$

where $b = P_3(0)$ can be obtained by solving a quadratic equation as mentioned in S2, $N = \frac{\pi}{\Delta\phi}$, $j = \frac{\phi}{\Delta\phi}$, $k_{Ab} = k_{Ab,0}\alpha^{-\pi}$. Even when $\phi_0 < \pi$, our solution gives a very good approximation if we set $P_1(j) \approx P_2(2N - j) \approx P_3(j) \approx 0 \quad \forall j \in (j_0, N]$.

As α is increased, this time-independent state becomes unstable giving rise to an oscillatory state. As described

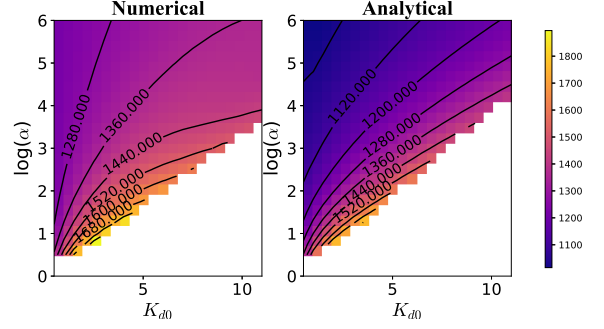


FIG. 5: Time period of oscillations for various α and K_{d0} i.e. at varying levels of differential affinity and % ATP. i.e. $k_1 = 0$. Other parameters are given in Table S1. Since, $k_1 = 0$, there is no effect of ultrasensitivity. The figure on the left represents time periods calculated by numerically simulating the FPE's. The figure on the right represents the time periods which were calculated from the imaginary part of the maximum positive eigenvalue of the instability matrix W , for small perturbations around the steady state probability distribution. As can be seen, the analytical solution provides us with a good approximation of the time period as well as the critical α at which oscillations take place for different K_{d0} . The contours in the figure are for the time period of oscillations.

in the S3, a linear stability analysis can be performed around the steady state of the system, \vec{P}^s to characterize this instability. The linear stability analysis has been detailed in S3 A. This analysis correctly predicts the observed oscillatory behavior. Indeed, in Fig. 5 we show that the analytical estimate of the time period of oscillations provides a very good description of the actual observed oscillation periods.

In the case of $k_1 \neq 0$ only an approximate solution for the time-independent steady state can be obtained. In order to obtain this approximate solution we take inspiration from the solution for the case when $k_1 = 0$ and assume $k_{Af}A_f P_1(\phi) = k_{Ab}\alpha^{\phi - \pi} P_3(\phi)$ for $\phi \in [0, \phi_0]$ (along the $P_1 - P_3$ connections in Fig. 2b) and $P_1(\phi) \approx 0 \approx P_3(\phi)$ for $\phi > \phi_0$. This assumption is supported by numerical evidence. Under this assumption, we obtain,

$$P_3(\phi) = P_3(\phi') \frac{|B + A\alpha^{\phi'}|}{|B + A\alpha^{\phi}|} \quad \forall \phi \in (0, \phi_0) \quad (3.4)$$

$$P_1(\phi) = \frac{K_{d0}}{A_f} \alpha^{\phi} P_3(\phi) \quad \forall \phi \in (0, \phi_0) \quad (3.5)$$

$$B = -k_0(1 - \gamma)\Delta\phi, \quad A = \frac{K_{d0}}{A_f} k_1(1 - \gamma_1)\Delta\phi \quad (3.6)$$

Here $P_3(0)$ can be obtained numerically and ϕ_0 denotes the place where $P_1 - P_2$ connections start in Fig. 2b. This is described in more detail in supplementary S2 B. Fig. S3b shows a comparison between the numerically obtained steady state with the one constructed using our

approximate solution. We also provide approximate analytical arguments to show how a linear instability analysis can again be used to characterize the onset of oscillations as k_1 is tuned. The Gershgorin circle theorem provides us with a way to understand where we can find the eigenvalues of any matrix. As k_1 is tuned, the -ve off-diagonal elements of the rate matrix \mathbf{W} increase in magnitude so do the radii of the Gershgorin discs (see Fig. S7) because for any transition rate matrix, \mathbf{M} , $\sum_i M_{ij} = 0$. In effect the Gershgorin discs have a finite area protruding into the positive half plane. With higher k_1 this area increases thus there is a higher chance of finding eigenvalues in the positive half-plane. These arguments are explained in more detail in S3 A.

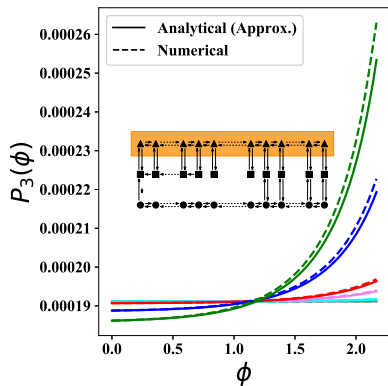


FIG. 6: Comparison between numerical and approximate analytical results for time-independent solution of P_3 states for the case when $k_1 \neq 0$ (3.4). The figure in the inset represents the Markov State network with the P_3 states highlighted. In the main figure, *grey* corresponds to $k_1 = 0$, *cyan* to $k_1 = 10^{-4}$, *violet* to $k_1 = 5 \times 10^{-4}$, *red* to $k_1 = 10^{-3}$, *blue* to $k_1 = 5 \times 10^{-3}$, *green* to $k_1 = 10^{-2}$.

In the next section, we build on these results and show how ultrasensitivity and differential affinity can support oscillations even at a lower ATP concentration. We also use insight from these analytical arguments to explain how the time period can be stably maintained in a variety of ATP concentrations, a phenomena known as affinity compensation. Finally, using our minimal model, we also comment on the thermodynamic costs associated with maintaining oscillations.

IV. DISCUSSION

A. Increasing Differential Affinity leads to oscillations at low %ATP

It has been numerically shown previously in [21] that oscillations in a model system similar to ours can be obtained by increasing the value of α i.e. by improving the differential affinity. α controls the rate of reaction between P_1 and P_3 states in Fig. 2b. Our analytical

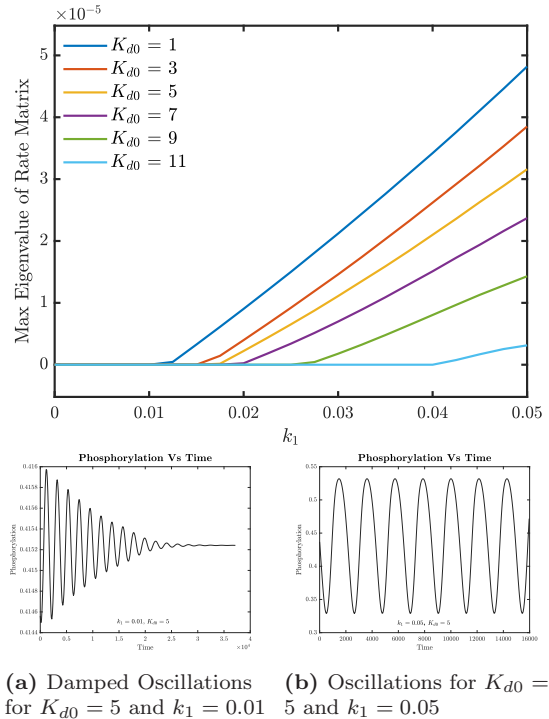


FIG. 7: Instability leading to oscillations when changing k_1 . The y-axis denotes the maximum eigenvalue of the rate matrix \mathbf{W} for the perturbations (refer to supplementary). The presence of a +ve eigenvalue denotes that the time-independent steady state is unstable. $\alpha = 10$ and the other parameter values are listed in Table S2

results explain this numerical observation. Further, our analytical results at $k_1 = 0$ also help predict the required interplay between α and the ATP concentration in order for oscillations to be sustained. Specifically, we find that at $k_1 = 0$, a higher value of α is required for oscillations to take place at higher K_{d0} (or a lower ATP concentration). In Fig. 8 we provide estimates of how the critical value of α changes as a function of the K_{d0} . Our analytical estimates agree very well with those obtained from the numerical calculations.

B. Improving the ultrasensitive response leads to oscillations at lower %ATP and fixed Differential Affinity

As mentioned in section II, it has been speculated that ultrasensitivity plays an important role in sustaining oscillations at low %ATP conditions. Our minimal model captures this role played by ultrasensitivity. Indeed, we find that at a higher value of k_1 , corresponding to a sharper ultrasensitive response (Fig. 3), oscillations can be sustained a larger K_{d0} (or a smaller ATP concentration). We describe this tradeoff in Fig.7 and Fig. 9.

Our analytical analysis also allows us to provide a phe-

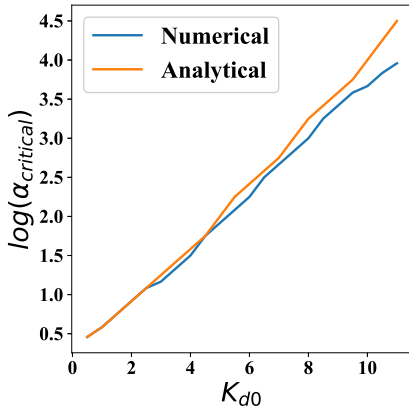


FIG. 8: The value of α required for the onset of oscillations as a function of K_{d0} . Estimates have been obtained both from our theory and from numerical simulations. We set $k_1 = 0$ for these calculations.

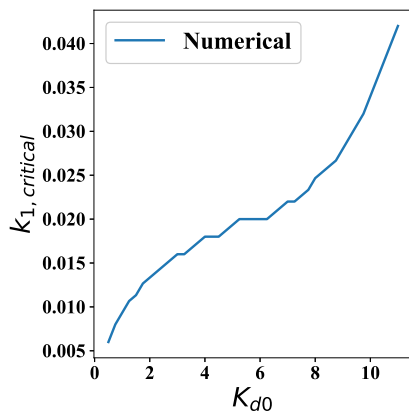


FIG. 9: The value of k_1 required for the onset of oscillations as a function of K_{d0} . Since the $k_1 \neq 0$ is only approximately tractable analytically, we have only plotted estimates from numerical simulations.

nomenological understanding of the role played by the ultrasensitive switch. Ultrasensitivity offers coherence to the travelling wave-packet of phosphorylation at the start of every new cycle of oscillation. Phosphorylation is halted until a critical amount of KaiA is present in the system. Just before the beginning of every new phosphorylation cycle, most of the KaiA is sequestered by the P_2 states. Only after a certain amount of KaiA is freed from P_2 states, the phosphorylation reactions in the P_3 states can start again. This leads to a buildup of probability density near $P_2(2\pi)$ and $P_1(0)$ before the start of every cycle and provides coherence to the system and oscillations can be sustained.

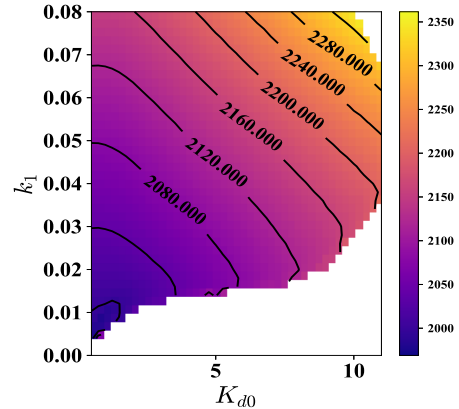


FIG. 10: Time Period of oscillations for various K_{d0} and k_1 i.e. at different levels of % ATP and ultrasensitivity. The white region denotes the parameter space which does not support oscillations. This is also supported by the plot for the amplitude of oscillations, Fig. 11. In order to have oscillations at higher values of K_{d0} the system requires a higher value of k_1 . The contours in the figure are for the time period of oscillations.

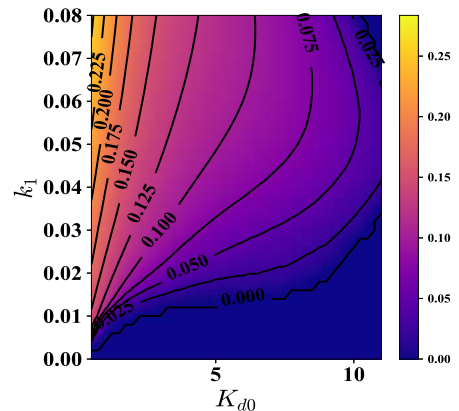


FIG. 11: Amplitude of oscillations as a function of K_{d0} and k_1 at $\alpha = 10$ and parameters given in S2. The contours in the figure are for the amplitude of oscillations.

C. Metabolic compensation of Time period: Insights from the minimal Markov state model

One of the most important feature of the KaiABC oscillator is that the time period of the oscillations are robust to changes in the %ATP in the system, a phenomenon known as metabolic compensation. Our model shows a similar behaviour. Upon increasing K_{d0} , the time period increases, changing by 10% for an increase from $K_{d0} = 1$ to 11 (see Fig. 10 and Fig. 12). At $K_{d0} > 11$, oscillations are not supported. This is analogous to losing oscillations when %ATP is below 20%ATP in the real system[10, 14].

Our minimal model helps provide a simple phenomenological explanation of affinity compensation. In the

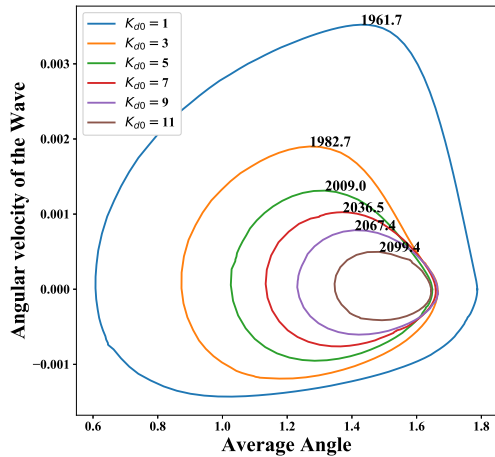


FIG. 12: Velocity of Phosphorylation wavepacket as a function of Average Angle for $k_1 = 0.05$, various K_{d0} 's and other parameters as given in Table. S2. Here Average Angle, $\langle \phi \rangle = \sum_{\phi} \phi P(\phi)$ and Velocity, $v = \frac{d\langle \phi \rangle}{dt}$. The time period of oscillation for the different cycles is denoted along the curves.

regime where our model allows oscillations, the speed of the wave form as it traverses the top $P_1 - P_3$ rungs in Fig.2b from regions of lower ϕ to regions of higher ϕ can be shown to be $v = \frac{1}{3} \frac{(1-\gamma)k_0 - cK_{d0}(1-\gamma)k_1}{1+cK_{d0}}$ through a first-passage time analysis (outlined in Sec. S4). Thus it is expected to decrease with K_{d0} . Simultaneously, $1/K_{d0} \equiv k_{Af}/k_{Ab,0}$ can be expected to control the relative occupancy of the $P_1 - P_3$ states and the transitions in the P_3 states promote probability flux towards regions of higher ϕ . Thus, with increasing $1/K_{d0}$, the waveform can be expected to traverse more of the large ϕ states in the P_3 rung before transitioning to the P_1 and then eventually to the P_2 states as it restarts the oscillation. Hence, at higher $1/K_{d0}$ or higher %ATP, the system traverses a larger orbit as described in the 'Angle-Angular Velocity' phase space (Fig. 12). This is analogous to shifting in the trough and crest in the phosphorylation oscillations observed in the KaiABC system [10]. Together, these effects make the time period of oscillations relatively insensitive to %ATP levels (Fig. 12). In this way, the KaiABC system can accomplish affinity compensation and maintain a relatively constant time period.

D. The thermodynamic costs of setting up oscillations

Finally, the stochastic thermodynamics of our minimal model can be readily probed. The total steady state entropy production rate can be estimated using the prob-

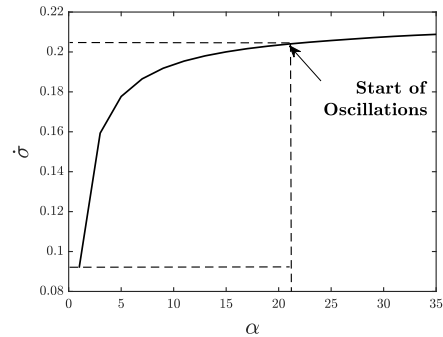


FIG. 13: Entropy Production Rate Vs α for $K_{d0} = 5, k_1 = 0$ and other parameters given in Table.S1. Oscillations start at $\alpha = 21$. $\alpha = 1$ corresponds to absence of differential affinity. In order to have oscillations an additional 0.113 units of energy are required. This energy goes into building coherence among the KaiABC oscillator population [21]

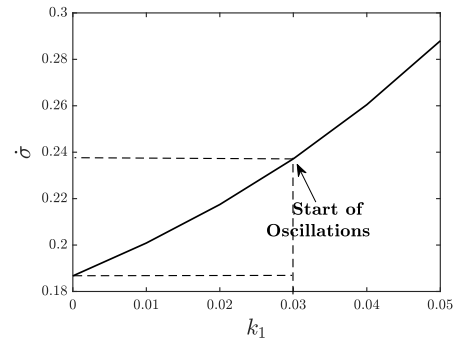


FIG. 14: Entropy Production Rate Vs k_1 for $\alpha = 10, K_{d0} = 8$ and other parameters given in Table.S2. Unlike the case with changing α in Fig. 13 where the entropy production plateaus very quickly with increasing α , in this case, the entropy production increases almost linearly with increasing k_1 . As expected, decreasing K_{d0} and increasing k_1 lead to higher dissipation of energy. Oscillations start at $k_1 = 0.03$. $k_1 = 0$ corresponds to absence of ultrasensitivity in the system. An additional 0.052 units of energy are dissipated in order to have oscillations. This additional energy goes into improving the ultrasensitive response of the system eventually leading to coherence.

ability fluxes along every edge of the model as [27]

$$\dot{\sigma} = \sum_{Edges} (J_+ - J_-) \ln \frac{J_+}{J_-} \quad (4.1)$$

We use Eq. 4.1 to estimate the entropy production rate for various values of α , K_{d0} and k_1 . These results are described in Fig. 13 and Fig. 14. Of particular note, our results show that $\dot{\sigma}$ varies continuously through the transition of the system from a stationary to an oscillatory phase. In the case where the ultrasensitivity parameter k_1 is tuned (Fig. 14), the entropy production rate, $\dot{\sigma}$ is almost a linearly increasing function of k_1 . While the entropy production rate, $\dot{\sigma}$ does indeed increase as os-

cillations are setup in agreement with previous studies, [21], and it does indeed improve the overall quality and coherence of oscillation [28, 29] an analysis focused on just the entropy production rate might miss the important and specific roles played by biophysical mechanisms such as the ultrasensitivity and differential affinity in promoting and sustaining robust oscillations [30].

V. CONCLUSION

In conclusion, this work elucidates the role played by biophysical mechanisms such as ultrasensitivity and dif-

ferential affinity in controlling the quality of circadian oscillations. Our minimal theoretical model also provides a route to explain how biochemical circuits can ensure oscillations with constant time periods, even under a range of experimental conditions. Finally, we show that the net rate of energy dissipation isn't a very effective order parameter to gauge the quality of oscillations, particularly in regimes where the ultrasensitivity is important. While our work relies on a very minimal abstraction of the KaiABC system. In future work we hope to adapt these ideas to more complex and complete models of circadian rhythm oscillators.

-
- [1] Jennifer A. Mohawk, Carla B. Green, and Joseph S. Takahashi. Central and peripheral circadian clocks in mammals. *Annual Review of Neuroscience*, 35(1):445–462, 2012. PMID: 22483041.
- [2] Takao Kondo and Masahiro Ishiura. The circadian clock of cyanobacteria. *BioEssays*, 22(1):10–15, 2000.
- [3] Justin Blau. The drosophila circadian clock: what we know and what we don't know. *Seminars in Cell & Developmental Biology*, 12(4):287–293, 2001.
- [4] Ben Collins and Justin Blau. Keeping time without a clock. *Neuron*, 50(3):348–350, 2006.
- [5] Jeanne F. Duffy and Jr. Kenneth P. Wright. Entrainment of the human circadian system by light. *Journal of Biological Rhythms*, 20(4):326–338, 2005. PMID: 16077152.
- [6] Christine Dubowy and Amita Sehgal. Circadian Rhythms and Sleep in *Drosophila melanogaster*. *Genetics*, 205(4):1373–1397, 04 2017.
- [7] Bruno M. C. Martins, Amy K. Tooke, Philipp Thomas, and James C. W. Locke. Cell size control driven by the circadian clock and environment in cyanobacteria. *Proceedings of the National Academy of Sciences*, 115(48):E11415–E11424, 2018.
- [8] Yan Ouyang, Carol R. Andersson, Takao Kondo, Susan S. Golden, and Carl Hirschie Johnson. Resonating circadian clocks enhance fitness in cyanobacteria. *Proceedings of the National Academy of Sciences*, 95(15):8660–8664, 1998.
- [9] Yi Liao and Michael J. Rust. The circadian clock ensures successful dna replication in cyanobacteria. *Proceedings of the National Academy of Sciences*, 118(20), 2021.
- [10] Connie Phong, Joseph S. Markson, Crystal M. Wilhoite, and Michael J. Rust. Robust and tunable circadian rhythms from differentially sensitive catalytic domains. *Proceedings of the National Academy of Sciences of the United States of America*, 110(3):1124–1129, 2013.
- [11] Sébastien Clodong, Ulf Dühring, Luiza Kronk, Annegret Wilde, Ilka Axmann, Hanspeter Herzog, and Markus Kollmann. Functioning and robustness of a bacterial circadian clock. *Molecular Systems Biology*, 3(1):90, 2007.
- [12] Paula Avello, Seth J. Davis, and Jonathan W. Pitchford. Temperature robustness in arabidopsis circadian clock models is facilitated by repressive interactions, autoregulation, and three-node feedbacks. *Journal of Theoretical Biology*, 509:110495, 2021.
- [13] Andrey A. Dovzhenok, Mokryun Baek, Sookkyung Lim, and Christian I. Hong. Mathematical modeling and validation of glucose compensation of the neurospora circadian clock. *Biophysical Journal*, 108(7):1830–1839, 2015.
- [14] Joris Paijmans, David K. Lubensky, and Pieter Rein ten Wolde. A thermodynamically consistent model of the post-translational kai circadian clock. *PLOS Computational Biology*, 13(3):1–43, 03 2017.
- [15] Michael J. Rust, Susan S. Golden, and Erin K. O'Shea. Light-driven changes in energy metabolism directly entrain the cyanobacterial circadian oscillator. *Science*, 331(6014):220–223, 2011.
- [16] Jun Tomita, Masato Nakajima, Takao Kondo, and Hideo Iwasaki. No transcription-translation feedback in circadian rhythm of kaic phosphorylation. *Science*, 307(5707):251–254, 2005.
- [17] Lu Hong, Danylo O Lavrentovich, Archana Chavan, Eugene Leypunskiy, and Eileen Li. Bayesian modeling reveals metabolite-dependent ultrasensitivity in the cyanobacterial circadian clock. *Molecular Systems Biology*, pages 1–23, 2020.
- [18] Tetsuhiro S. Hatakeyama and Kunihiko Kaneko. Reciprocity between robustness of period and plasticity of phase in biological clocks. *Physical Review Letters*, 115(21):1–5, 2015.
- [19] Taeko Nishiwaki, Yoshinori Satomi, Masato Nakajima, Cheolju Lee, Reiko Kiyohara, Hakuto Kageyama, Yohko Kitayama, Mioko Temamoto, Akihiro Yamaguchi, Atsushi Hijikata, Mitiko Go, Hideo Iwasaki, Toshifumi Takao, and Takao Kondo. Role of kaic phosphorylation in the circadian clock system of *synechococcus elongatus* pcc 7942. *Proceedings of the National Academy of Sciences*, 101(38):13927–13932, 2004.
- [20] Michael J. Rust. Orderly wheels of the cyanobacterial clock. *Proceedings of the National Academy of Sciences*, 109(42):16760–16761, 2012.
- [21] Dongliang Zhang, Yuansheng Cao, Qi Ouyang, and Yuhai Tu. The energy cost and optimal design for synchronization of coupled molecular oscillators. *Nature Physics*, 16(1):95–100, 2020.
- [22] Taeko Nishiwaki and Takao Kondo. Circadian autodephosphorylation of cyanobacterial clock protein kaic occurs via formation of atp as intermediate*. *Journal of Biological Chemistry*, 287(22):18030–18035, 2012.

- [23] Jeroen S. van Zon, David K. Lubensky, Pim R. H. Altena, and Pieter Rein ten Wolde. An allosteric model of circadian kaic phosphorylation. *Proceedings of the National Academy of Sciences*, 104(18):7420–7425, 2007.
- [24] A Goldbeter and D E Koshland. An amplified sensitivity arising from covalent modification in biological systems. *Proceedings of the National Academy of Sciences*, 78(11):6840–6844, 1981.
- [25] James E Ferrell Jr and Sang Hoon Ha. Ultrasensitivity part I : Michaelian responses and zero-order ultrasensitivity. *Trends in Biochemical Sciences*, 39(10):496–503, 2014.
- [26] Stefan Legewie, Nils Blüthgen, and Hanspeter Herzl. Quantitative analysis of ultrasensitive responses. *FEBS Journal*, 272(16):4071–4079, 2005.
- [27] Hong Qian. Phosphorylation energy hypothesis: Open chemical systems and their biological functions. *Annual Review of Physical Chemistry*, 58(1):113–142, 2007. PMID: 17059360.
- [28] Basile Nguyen, Udo Seifert, and Andre C. Barato. Phase transition in thermodynamically consistent biochemical oscillators. *The Journal of Chemical Physics*, 149(4):045101, 2018.
- [29] Clara del Junco and Suriyanarayanan Vaikuntanathan. High chemical affinity increases the robustness of biochemical oscillations. *Phys. Rev. E*, 101:012410, Jan 2020.
- [30] Daniel S. Seara, Benjamin B. Machta, and Michael P. Murrell. Irreversibility in dynamical phases and transitions. *Nature Communications*, 12(1):1–9, 2021.

SUPPLEMENTARY INFORMATION

S1. MODEL DETAILS

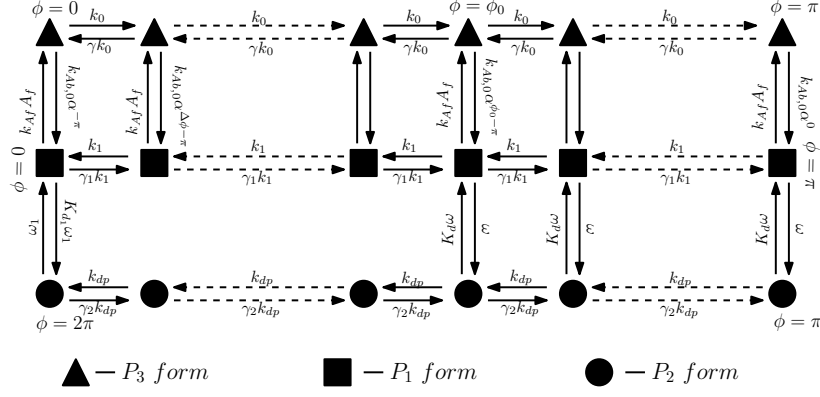


FIG. S1: Each oscillator can exist in one of the three forms P_1, P_2, P_3 . The P_1 form corresponds to normal KaiC during daytime and requires KaiA for moving forward in phase. The P_3 form corresponds to the form of KaiC to which KaiA is attached as an assistant molecule, $P_1 + KaiA \rightarrow P_3$. The P_2 form corresponds to KaiC in its dephosphorylation phase. The nucleotide bound states, KaiB binding and KaiA sequestration are implicitly assumed in the model. A_f denotes the free KaiA concentration and A_t stands for the total KaiA concentration. Phosphorylation corresponds to phase ϕ , it increases linearly from 0 to 1 as ϕ varies from 0 to π and decreases linearly from 1 to 0 as ϕ goes from π to 2π . Connections between the P_1 states denote the spontaneous dephosphorylation of KaiC subunits in the absence of KaiA. Multiple connections between P_1 and P_2 towards the highly phosphorylated states allows the system to move to the dephosphorylation phase even before all the KaiC is completely phosphorylated. The P_2 states sequester KaiA which corresponds to the fact that during the dephosphorylation phase, KaiB bound KaiC sequesters KaiA and makes it inactive. The master equation for this system is given below.

$$\begin{aligned} \frac{\partial P_1(\phi)}{\partial t} &= \delta(\phi \neq \pi)k_1(P_1(\phi + \Delta\phi) - \gamma_1 P_1(\phi)) + \delta(\phi \neq 0)k_1(\gamma_1 P_1(\phi - \Delta\phi) - P_1(\phi)) \\ &\quad + \delta(\phi)(\omega_1 P_2(2\pi - \phi) - K_{d1}\omega_1 P_1(\phi)) \\ &\quad + H(\phi - \phi_0)(K_d\omega P_2(2\pi - \phi) - \omega P_1(\phi)) - k_{A_f}A_f P_1(\phi) + k_{A_b,0}\alpha^{\phi-\pi} P_3(\phi) \end{aligned} \quad (S1.1)$$

$$\begin{aligned} \frac{\partial P_2(\phi)}{\partial t} &= \delta(\phi \neq 2\pi)k_{dp}(\gamma_2 P_2(\phi + \Delta\phi) - P_2(\phi)) + \delta(\phi \neq \pi)k_{dp}(P_2(\phi - \Delta\phi) - \gamma_2 P_2(\phi)) \\ &\quad - \delta(\phi - 2\pi)(\omega_1 P_2(\phi) - K_{d1}\omega P_1(\phi - 2\pi)) + H(2\pi - \phi - \phi_0)(\omega P_1(2\pi - \phi) - \omega P_2(\phi)) \end{aligned} \quad (S1.2)$$

$$\begin{aligned} \frac{\partial P_3(\phi)}{\partial t} &= \delta(\phi \neq \pi)k_0(\gamma P_3(\phi + \Delta\phi) - P_3(\phi)) + \delta(\phi \neq 0)k_0(P_3(\phi - \Delta\phi) - \gamma P_3(\phi)) \\ &\quad + k_{A_f}A_f P_1(\phi) - k_{A_b,0}\alpha^{\phi-\pi} P_3(\phi) \end{aligned} \quad (S1.3)$$

$$A_f = A_t - \sum_0^\pi P_3(\phi) - \epsilon_{seq} \sum_\pi^{2\pi} P_2(\phi), \quad \epsilon_{seq} < A_t \quad (S1.4)$$

$$\begin{aligned} \frac{dA_f}{dt} &= \sum_0^\pi (k_{A_b,0}\alpha^{\phi-\pi} P_3(\phi) - k_{A_f}A_f P_1(\phi)) \\ &\quad + \epsilon_{seq} \sum_\pi^{2\pi} (H(2\pi - \phi - \phi_0)\omega P_2(\phi) - K_d\omega P_1(2\pi - \phi)) + \epsilon(\omega_1 P_2(2\pi) - K_{d1}\omega_1 P_1(0)) \end{aligned} \quad (S1.5)$$

$$H(\phi) = 1 \text{ for } \phi \geq 0 \text{ and } 0 \text{ for } \phi < 0 \quad (S1.6)$$

For the sake of convenience, we relabel the P_2 states such that $P_2(2N - j) \iff P_2(j)$. We also work with the discrete case so we relabel the ϕ using j , where $j = \frac{\phi}{\Delta\phi}$. Relabelling does not change the dynamics. The Fokker-

Planck equations in this case are given by,

$$\begin{aligned} \frac{\partial P_1(j)}{\partial t} &= \delta(j \neq N)k_1(P_1(j+1) - \gamma_1 P_1(j)) + \delta(j \neq 0)k_1(\gamma_1 P_1(j-1) - P_1(j)) \\ &\quad + \delta(j=0)(\omega_1 P_2(j) - K_{d1}\omega_1 P_1(j)) \\ &\quad + H(j-j_0)(K_d\omega P_2(j) - \omega P_1(j)) - k_{Af}A_f P_1(j) + k_{Ab}\alpha^j P_3(j) \end{aligned} \quad (S1.7)$$

$$\begin{aligned} \frac{\partial P_2(j)}{\partial t} &= \delta(j \neq 0)k_{dp}(\gamma_2 P_2(j-1) - P_2(j)) + \delta(j \neq N)k_{dp}(P_2(j+1) - \gamma_2 P_2(j)) \\ &\quad - \delta(j=0)(\omega_1 P_2(j) - K_{d1}\omega_1 P_1(j)) + H(j-j_0)(\omega P_1(j) - \omega P_2(j)) \end{aligned} \quad (S1.8)$$

$$\begin{aligned} \frac{\partial P_3(j)}{\partial t} &= \delta(j \neq N)k_0(\gamma P_3(j+1) - P_3(j)) + \delta(j \neq 0)k_0(P_3(j-1) - \gamma P_3(j)) \\ &\quad + k_{Af}A_f P_1(j) - k_{Ab}\alpha^j P_3(j) \end{aligned} \quad (S1.9)$$

$$A_f = A_t - \sum_0^N P_3(j) - \epsilon_{seq} \sum_0^N P_2(j) \quad (S1.10)$$

S2. TIME INDEPENDENT STEADY STATE

A. Case I : $k_1 = 0$

We set, $k_1 = 0, j_0 = N, K_{d1} = K_d = K_D$, we also make the following changes in notation $k_{Ab,0}\alpha^{-\pi} = k_{Ab}, k_{dp} = k_2, \alpha- > \alpha^{\frac{\pi}{N}}$. Using this simplification, we can solve for the steady state solution of the system and then use linear stability analysis around the steady state to see how oscillations are set up.

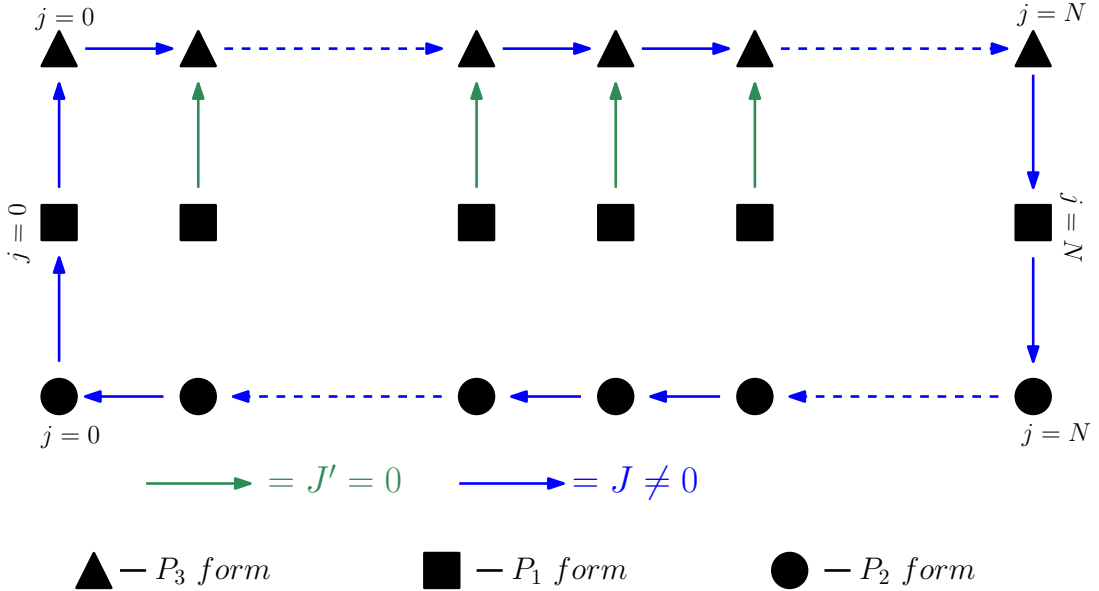


FIG. S2: There is just one flux, J in the entire system. Once we solve for this unique flux J , we can obtain the expressions for the probability distribution of the different states in the system.

$$A_f = A_t - \epsilon \sum_{j=0}^N P_3(j), \quad P_3(0) = b, \quad P_1(0) = a \quad (S2.1)$$

where a and b are the labels for $P_1(0)$ and $P_3(0)$ respectively. For the $P_1 - P_3$ connection at $j = 0$ and $j = N$ we have,

$$J = k_{Af}A_fP_1(0) - k_{Ab}\alpha^0P_3(0) = k_{Af}A_fa - k_{Ab}b \quad (\text{S2.2})$$

$$J = k_{Ab}\alpha^N P_3(N) - k_{Af}A_fP_1(N) \quad (\text{S2.3})$$

For other $P_3 - P_3$ connections, we have,

$$J = k_0P_3(j-1) - \gamma k_0P_3(j) \quad (\text{S2.4})$$

$$\implies P_3(j) = \frac{1}{\gamma k_0} [k_0P_3(j-1) - J] \quad (\text{S2.5})$$

$$\therefore P_3(1) = \frac{1}{\gamma k_0} [k_0b - J], \quad P_3(j) = \frac{1}{\gamma k_0} \left[\frac{k_0}{\gamma^{j-1}}b - J \left(1 + \frac{1}{\gamma} + \dots + \frac{1}{\gamma^{j-1}} \right) \right] \quad (\text{S2.6})$$

$$\implies P_3(j) = \frac{1}{\gamma k_0} \left[\frac{k_0}{\gamma^{j-1}}b - J \left(\frac{1 - \frac{1}{\gamma^j}}{1 - \frac{1}{\gamma}} \right) \right] \quad (\text{S2.7})$$

If we look at $P_1 - P_3$ connections in the bulk, we have,

$$J' = 0 \implies k_{Af}A_fP_1(j) = k_{Ab}\alpha^j P_3(j) \quad \forall j \neq 0, N \quad (\text{S2.8})$$

When we look at the $P_1 - P_2$ connection at $j = 0$, we have,

$$J = \omega_1P_2(0) - K_D\omega_1P_1(0) \implies P_2(0) = \frac{1}{\omega_1} [J + K_{d1}\omega_1a] = c \quad (\text{S2.9})$$

where c is the label for $P_2(0)$. Similarly for other $P_2 - P_2$ connections we have the following,

$$J = k_2P_2(j) - \gamma_2k_2P_2(j-1) \quad (\text{S2.10})$$

$$\implies P_2(1) = \frac{1}{k_2} [J + \gamma_2k_2c], \quad P_2(j) = \frac{1}{k_2} \left[\gamma_2^j k_2c + J(1 + \gamma_2 + \dots + \gamma_2^{j-1}) \right] \quad (\text{S2.11})$$

$$\implies P_2(j) = \frac{1}{k_2} \left[\gamma_2^j k_2c + J \frac{1 - \gamma_2^j}{1 - \gamma_2} \right] \quad (\text{S2.12})$$

$$(\text{S2.13})$$

Substituting the expressions of $P_1(N)$ (S2.3), $P_2(N)$ (S2.12) and $P_3(N)$ (S2.7) into (S2.14), we get,

$$\text{At } j = N, \quad k_{Ab}\alpha^N P_3(N) - k_{Af}A_fP_1(N) = J = \omega P_1(N) - K_D\omega P_2(N) \quad (\text{S2.14})$$

$$\implies \frac{k_{Ab}\alpha^N}{\gamma^N} - k_{Af}A_fK_dK_{d1}\gamma_2^N a = \left[1 + \frac{k_{Af}A_f}{\omega_1} + \frac{k_{Af}A_fK_d}{k_2} \frac{1 - \gamma_2^N}{1 - \gamma_2} + \frac{k_{Ab}\alpha^N}{\gamma k_0} \frac{1 - \frac{1}{\gamma^N}}{1 - \frac{1}{\gamma}} + \frac{k_{Af}A_fK_d\gamma_2^N}{\omega} \right] J \quad (\text{S2.15})$$

$$J = k_{Af}A_fa - k_{Ab}b \quad (\text{S2.16})$$

Since N is large and $\gamma < 1$, the LHS and RHS (S2.15) are dominated by the terms having $\frac{1}{\gamma^N}$. Thus only the 1st term in the LHS and the 3rd term in the RHS of (S2.15) contribute, other terms can be ignored. This leads to an expression for J.

$$\implies J = k_0(1 - \gamma)b \quad (\text{S2.17})$$

Substituting this expression for J in (S2.7), (S2.12), (S2.2), (S2.3), (S2.14), we get,

$$\therefore P_3(j) = b\forall j \quad (\text{S2.18})$$

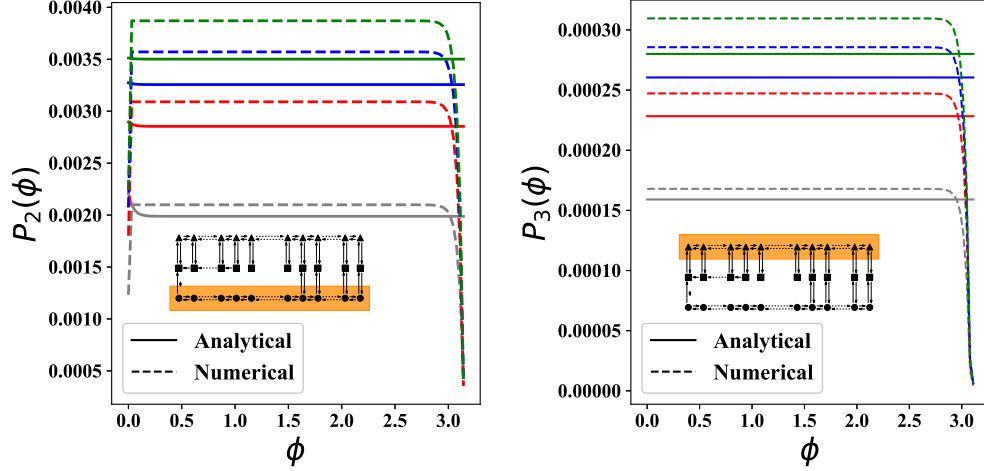
$$P_1(j) = \frac{1}{k_{Af}A_f} [k_{Ab}\alpha^j + (\delta_{0,j} - \delta_{N,j})k_0(1 - \gamma)] b \quad (\text{S2.19})$$

$$P_2(j) = \frac{k_0}{k_2} \left(\frac{1 - \gamma}{1 - \gamma_2} \right) b + \gamma_2^j \left[k_0(1 - \gamma) \left(\frac{1}{\omega_1} - \frac{1}{k_2(1 - \gamma_2)} \right) + \frac{K_{d1}\omega}{k_{Af}A_f\omega_1} (k_0(1 - \gamma) + k_{Ab}) \right] b \quad (\text{S2.20})$$

Now using, $\sum_{j=0}^N (P_1(j) + P_2(j) + P_3(j)) = 1$,

$$\begin{aligned} \Rightarrow \frac{1}{b} = \frac{1}{k_{Af}A_f} & \left[k_{Ab} \frac{\alpha^{N+1} - 1}{\alpha - 1} + \frac{K_{d1}\omega(k_0(1-\gamma) + k_{Ab})}{(1-\gamma_2)\omega_1} \right] \\ & + (N+1) \left(1 + \frac{k_0(1-\gamma)}{k_2(1-\gamma_2)} \right) + \frac{1}{1-\gamma_2} \left(k_0 \left(\frac{1-\gamma}{\omega_1} \right) - \frac{k_0(1-\gamma)}{k_2(1-\gamma_2)} \right) \end{aligned} \quad (\text{S2.21})$$

$A_f = A_t - \epsilon \sum_{j=0}^N P_3(j) - \epsilon_{seq} \sum_{j=0}^N P_3(j) = A_t + f - gb$, where f and g are constants. Setting $\epsilon_{seq} = 0$, we get, $A_f = A_t - (N+1)b$ and we need to solve a quadratic equation to find the probabilities which determine the steady state.



(a) Comparison between numerical and analytical results for time-independent solution of P_2 states. The figure in inset is a representation of the Markov State network with the P_1 states highlighted.

(b) Comparison between numerical and analytical results for time-independent solution of P_3 states. The figure in inset is a representation of the Markov State network with the P_1 states highlighted.

FIG. S3: In the main figures, *grey* corresponds to $\alpha = 2$, *red* to $\alpha = 4$, *blue* to $\alpha = 6$ and *green* to $\alpha = 8$

B. Case II : $k_1 \neq 0$

The case with $k_1 \neq 0$ is challenging to solve. Unlike the previous case, where only a single flux existed in the entire system, in this case there will be many fluxes in the system.

In order to obtain the rough form of solution for P_1 , P_2 and P_3 states, we make some assumptions which are supported by numerical observations. We also go the continuum limit where the discrete master equations describing the system become a set of coupled PDE's. The boundaries for our problem are $x = 0$ and $x = x_0$. x_0 is the point where the $P_1 - P_2$ connections start. Numerically it is observed that at the steady state, the probability density in the states beyond x_0 is negligible compared to the ones before it. Thus we set it as our boundary. We solve the problem for the states in the bulk and then impose certain conditions such that the boundary conditions are satisfied.

$$\begin{aligned} \frac{\partial P_1(x)}{\partial t} = & \delta(x \neq N)k_1(P_1(x + \Delta x) - \gamma_1 P_1(x)) + \delta(x \neq 0)k_1(\gamma_1 P_1(x - \Delta x) - P_1(x)) \\ & + \delta(x = 0)(\omega_1 P_2(x) - K_{d1}\omega_1 P_1(x)) \\ & + H(x - x_0)(K_d\omega P_2(x) - \omega P_1(x)) - k_{Af}A_f P_1(j) + k_{Ab}\alpha^x P_3(j) \end{aligned} \quad (\text{S2.22})$$

$$(\text{S2.23})$$

and so on and so forth for P_2 and P_3 states. Using Taylor expansion, $P(x + \Delta x) = P(x) + \frac{\partial P(x)}{\partial x}\Delta x + \frac{1}{2}\frac{\partial^2 P(x)}{\partial x^2}\Delta x^2 +$

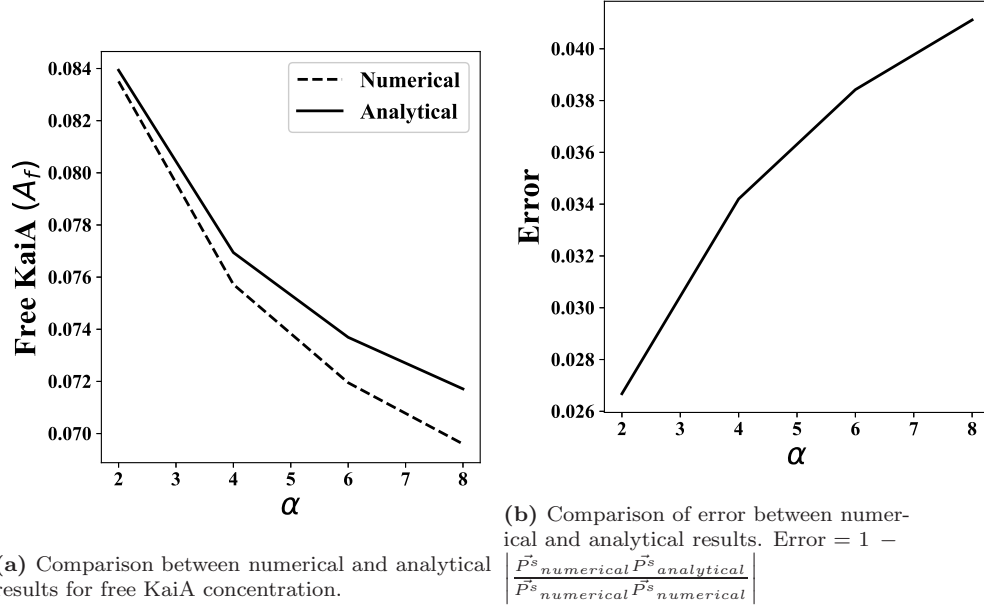


FIG. S4: Comparison of free KaiA concentration and error between the analytical data and numerical data.

$O(\Delta x^3)$, we get,

$$\frac{\partial P_1(x)}{\partial t} = k_{1c} \frac{\partial P_1(x)}{\partial x} + k_{1d} \frac{\partial^2 P_1(x)}{\partial x^2} - k_{Af} A_f P_1(x) + k_{Ab} \alpha^x P_3(x) \quad (\text{S2.24})$$

$$\frac{\partial P_2(x)}{\partial t} = k_{2c} \frac{\partial P_2(x)}{\partial x} + k_{2d} \frac{\partial^2 P_2(x)}{\partial x^2} \quad (\text{S2.25})$$

$$\frac{\partial P_3(x)}{\partial t} = k_{3c} \frac{\partial P_3(x)}{\partial x} + k_{3d} \frac{\partial^2 P_3(x)}{\partial x^2} + k_{Af} A_f P_1(x) - k_{Ab} \alpha^x P_3(x) \quad (\text{S2.26})$$

$$k_{1c} = k_1(1 - \gamma_1)\Delta x, \quad k_{2c} = k_{dp}(1 - \gamma_2)\Delta x, \quad k_{3c} = -k_0(1 - \gamma)\Delta x \quad (\text{S2.27})$$

$$k_{1d} = \frac{1}{2}k_1(1 + \gamma_1)\Delta x^2, \quad k_{2d} = \frac{1}{2}k_{dp}(1 + \gamma_2)\Delta x^2, \quad k_{3d} = \frac{1}{2}k_0(1 + \gamma)\Delta x^2 \quad (\text{S2.28})$$

We begin with the ansatz that when k_1 is increased from 0 to a very small number gradually, the changes in the form of the probability distribution will not change drastically. Keeping this in mind we make the assumption, $k_{Af} A_f P_1(x) \approx k_{Ab} \alpha^x P_3(x) \forall x \in Bulk$. This assumption has been inspired by our solution for the $k_1 = 0$ case and also supported by numerical observations. It can be better written as,

$$P_1(x) = \frac{K_{d0}}{A_f} \alpha^x P_3(x) \quad (\text{S2.29})$$

, where $K_{d0} = \frac{k_{Ab}}{k_{Af}}$. Thus, we have,

$$\partial_x P_1(x) = \frac{K_{d0}}{A_f} \alpha^x [\ln(\alpha) + \partial_x P_3(x)] \quad (\text{S2.30})$$

$$\partial_x^2 P_1(x) = \frac{K_{d0}}{A_f} \alpha^x [(\ln(\alpha))^2 P_3(x) + 2\ln(\alpha) \partial_x P_3(x) + \partial_x^2 P_3(x)] \quad (\text{S2.31})$$

Adding the evolution equations for P_1 and P_3 , in the bulk, and substituting the approximation (S2.29) we get,

$$\begin{aligned} \partial_t (P_1(x) + P_3(x)) &= \frac{K_{d0}}{A_f} \alpha^x \ln(\alpha) [k_{1c} + k_{1d} \ln(\alpha)] P_3(x) \\ &+ \left[k_{3c} + \frac{K_{d0}}{A_f} \alpha^x (k_{1c} + k_{1d} \ln(\alpha)) \right] \partial_x P_3(x) + \\ &+ \left[k_{3d} + \frac{K_{d0}}{A_f} \alpha^x k_{1d} \right] \partial_x^2 P_3(x) \end{aligned} \quad (\text{S2.32})$$

At steady state, $\partial_t P_1(x) = 0 = \partial_t P_3(x) \forall x$. For $k_1 = 0$, we have $k_{1c} = 0 = k_{1d}$. Thus we have the simple ODE,

$$k_{1c} \partial_x P_3(x) + k_{3d} \partial_x^2 P_3(x) = 0$$

This can have constant solutions for $P_3(x)$ and this is exactly what we have in the case when $k_1 = 0$ (S2.18). The presence of k_1 adds an extra term dependent on P_3 and due to this term we cannot have constant solutions for $P_3(x)$ (unless the constant solution is $P_3(x) = 0 \forall x$). Under the assumption that the form of $P_3(x)$ does not deviate significantly from the solution when $k_1 = 0$ ($P_3(x) = b = \text{constant}$), we can ignore terms containing $\partial_x^2 P_3(x)$. We also have $k_{3d} \ll k_{3c}$, $k_{1d} \ll k_{1c}$. Using this we can ignore terms containing k_{1d} and k_{3d} . Thus we finally arrive at the equation,

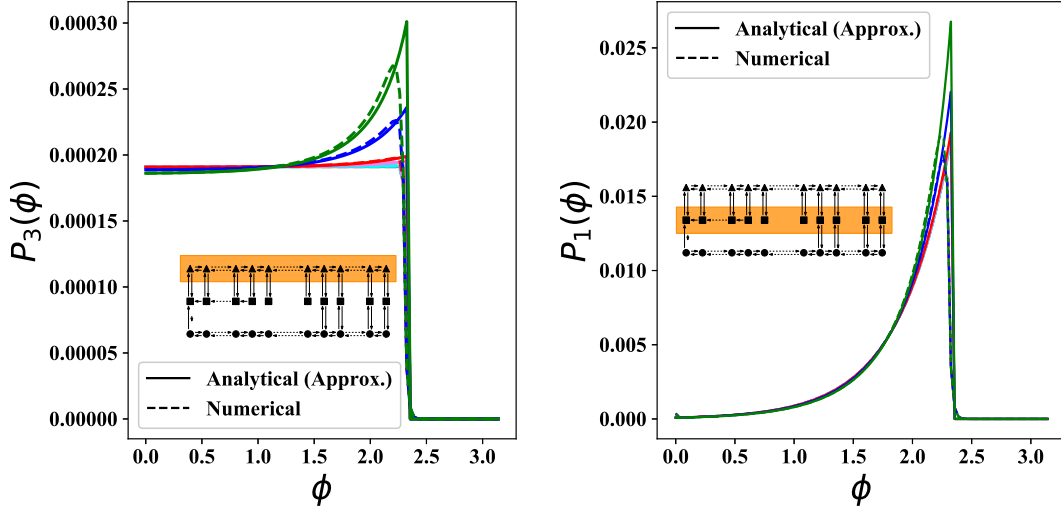
$$\frac{K_{d0}}{A_f} \alpha^x \ln(\alpha) k_{1c} P_3(x) + \left[k_{3c} + \frac{K_{d0}}{A_f} \alpha^x k_{1c} \right] \partial_x P_3(x) = 0 \quad (\text{S2.33})$$

$$\implies P_3(x) = P_3(x') \frac{|B + A\alpha^{x'}|}{|B + A\alpha^x|} \quad (\text{S2.34})$$

$$B = k_{3c}, \quad A = \frac{K_{d0}}{A_f} k_{1c} \quad (\text{S2.35})$$

Beyond the boundary at $x = x_0$, the network is constructed in such a way that it either drives the probabilities into the P_2 states which are further driven towards the boundary at x_0 from right or it drives the probabilities towards the boundary at x_0 in the P_1 states.

Thus we can safely assume that probability of the finding a state beyond the boundary at x_0 is close to 0. This is confirmed by numerical results. Now we can focus our entire attention to the region, $x \in [0, x_0]$. By using conservation of flux we can find the probabilities of all the other states.



(a) Comparison between numerical and analytical results for time-independent solution of P_3 states. The figure in inset is a representation of the Markov State network with the P_3 states highlighted.

(b) Comparison between numerical and analytical results for time-independent solution of P_1 states. The figure in inset is a representation of the Markov State network with the P_1 states highlighted.

FIG. S5: In the main figures, *grey* corresponds to $k_1 = 0$, *cyan* to $k_1 = 10^{-4}$, *violet* to $k_1 = 5 \times 10^{-4}$, *red* to $k_1 = 10^{-3}$, *blue* to $k_1 = 5 \times 10^{-3}$, *green* to $k_1 = 10^{-2}$.

C. Calculating Time-Independent Steady State numerically

As mentioned earlier, when $k_1 \neq 0$ and there are more than one connections between P_1 and P_2 states i.e. $j_0, x_0 \neq N$, we have multiple fluxes in the system. Nevertheless, we can still find the steady-state time-independent solution for \vec{P} irrespective of whether it is stable or not. An iterative procedure is adopted. The first step in this procedure is

to find the free KaiA concentration in the system. In the following paragraph the procedure is described. The set of FPE's that describe the evolution of \vec{P} can be expressed as, $\frac{\partial \vec{P}}{\partial t} = W(\vec{P})\vec{P}$, where \vec{P} is a vector of length $3N + 3$. The first $N+1$ elements would correspond to P_1 form, the next $N+1$ elements would correspond to P_2 form and the last $N+1$ elements would correspond to P_3 form. The rate matrix, W is function of the probabilities due to the presence of the A_f term which makes the entire thing non-linear. Now if we succeed in finding the free KaiA concentration at steady state, then substituting it back into W would make it a linear system to solve, and then $\frac{\partial \vec{P}}{\partial t} = W\vec{P}$. We can find A_f^s (free KaiA at steady state) using an iterative procedure as follows:

1. Initialize $A_f = A_t$ for the first run and form the rate matrix, W .
2. At steady state, $\frac{\partial \vec{P}}{\partial t} = 0 = W\vec{P}$. Compute the eigenvector corresponding to the nullspace of W and call it \vec{v}_0 .
3. Compute $A_f^{test} = A_t - \epsilon \sum_{i=2N+2}^{3N+2} v_0(i) - \epsilon_{seq} \sum_{i=N+1}^{2N+1} v_0(i)$
4. If $A_f^{test} < 0$, it would be unphysical. So set, $A_f^{new} = \frac{A_f^{old}}{2}$, else set $A_f^{new} = A_f^{old} + \delta(A_f^{test} - A_f^{old})$ where δ is some appropriate step size.
5. Repeat this procedure until convergence i.e. $\frac{|A_f^{old} - A_f^{test}|}{A_f^{old}} < Tolerance$

Once we have A_f^s we can find \vec{P}^s .

S3. LINEAR STABILITY ANALYSIS

We perturb around the steady state distribution, \vec{P}^s . Say, $P_k(j) = P_k^s(j) + \delta\eta_k(j)$, $k = 1, 2, 3$ and $j = 0, \dots, N$. By conservation of probability, we have $\sum_{k,j} \eta_k(j) = 0$. Substituting $P_k(j)$ in the differential equations, lead us to the evolution equations for $\eta_k(j)$.

$$\begin{aligned} \frac{\partial \eta_1(j)}{\partial t} &= \delta(j \neq N)k_1(\eta_1(j+1) - \gamma_1\eta_1(j)) + \delta(j \neq 0)k_1(\gamma_1\eta_1(j-1) - \eta_1(j)) \\ &\quad + \delta(j=0)(\omega_1\eta_2(j) - K_{d1}\omega_1\eta_1(j)) \\ &\quad + H(j-j_0)(K_d\omega\eta_2(j) - \omega\eta_1(j)) - k_{Af}A_f^s\eta_1(j) + k_{Ab}\alpha^j\eta_3(j) \\ &\quad + \epsilon k_{Af}P_1^s(j) \sum_{i=0}^N \eta_3(i) + \epsilon_{seq}k_{Af}P_1^s(j) \sum_{i=0}^N \eta_2(i) + O(\delta) \end{aligned} \quad (S3.1)$$

$$\begin{aligned} \frac{\partial \eta_2(j)}{\partial t} &= \delta(j \neq 0)k_{dp}(\gamma_2\eta_2(j-1) - \eta_2(j)) + \delta(j \neq N)k_{dp}(\eta_2(j+1) - \gamma_2\eta_2(j)) \\ &\quad - \delta(j=0)(\omega_1\eta_2(j) - K_{d1}\omega\eta_1(j)) \\ &\quad + H(j-j_0)(\omega\eta_1(j) - \omega\eta_2(j)) \end{aligned} \quad (S3.2)$$

$$\begin{aligned} \frac{\partial \eta_3(j)}{\partial t} &= \delta(j \neq N)k_0(\gamma\eta_3(j+1) - \eta_3(j)) + \delta(j \neq 0)k_0(\eta_3(j-1) - \gamma\eta_3(j)) \\ &\quad + k_{Af}A_f^s\eta_1(j) - k_{Ab}\alpha^j\eta_3(j) \\ &\quad - \epsilon k_{Af}P_1^s(j) \sum_{i=0}^N \eta_3(i) - \epsilon_{seq}k_{Af}P_1^s(j) \sum_{i=0}^N \eta_2(i) + O(\delta) \end{aligned} \quad (S3.3)$$

Notice the additional terms in evolution of $\vec{\eta}_1$ and $\vec{\eta}_3$ which are directly dependent on ϵ and ϵ_{seq} . The entire thing can be expressed as $\frac{\partial \vec{\eta}}{\partial t} = \tilde{\mathbf{W}}\vec{\eta} = (\mathbf{W} + \mathbf{W}')\vec{\eta}$. The entire matrix \tilde{W} can be broken into 9 parts, each representing interactions between different types of states as shown in (S3.5). The interesting blocks in the W -matrix are the $\eta_3 - \eta_3$ (S3.6) and $\eta_3 - \eta_2$ (S3.7) blocks which contain most of the terms arising due to nonlinearities.

In short, a linear stability analysis can be performed around the steady state of the system, \vec{P}^s , which yields upto first order,

$$\frac{\partial \vec{\eta}}{\partial t} = [\mathbf{W}(\vec{P}^s) + \nabla_{\vec{P}} \mathbf{W}(\vec{P}^s) \vec{P}^s] \vec{\eta} = [\mathbf{W}(\vec{P}^s) + \mathbf{W}'(\vec{P}^s)] \vec{\eta} = \tilde{\mathbf{W}} \vec{\eta} \quad (S3.4)$$

where η is the vector of perturbation (see Section S3 for a detailed expression). We work in a regime where the %ATP i.e. K_{d0} in our model plays a major role in deciding whether oscillations take place or not. The initial condition for every simulation is set to $P_1(0) = 1$ at $t=0$. This corresponds to starting all reactions with all the KaiC in the unphosphorylated and ADP bound form. The simulations are allowed to run for some time in order to reach either a time-independent or a time-dependent steady state behaviour. Now let us look at the \mathbf{W} matrix. It can be broken into 9 blocks,

$$\tilde{W} = \left(\begin{array}{c|c|c} W_{11} & W_{12} & W_{13} \\ \hline W_{21} & W_{22} & W_{23} \\ \hline W_{31} & W_{32} & W_{33} \end{array} \right) \quad (\text{S3.5})$$

$$W_{33} = \left(\begin{array}{ccc|ccc} -k_{Ab}\alpha^0 - \epsilon k_{Af} P_1^s(0) & -\epsilon k_{Af} P_1^s(0) & -\epsilon k_{Af} P_1^s(0) & \dots & \dots & -\epsilon k_{Af} P_1^s(0) \\ -\epsilon k_{Af} P_1^s(1) & -k_{Ab}\alpha^1 - \epsilon k_{Af} P_1^s(1) & -\epsilon k_{Af} P_1^s(1) & \dots & \dots & -\epsilon k_{Af} P_1^s(1) \\ \vdots & \dots & \ddots & \dots & \dots & \vdots \\ -\epsilon k_{Af} P_1^s(N-1) & \dots & -\epsilon k_{Af} P_1^s(N-1) & -k_{Ab}\alpha^{N-1} - \epsilon k_{Af} P_1^s(N-1) & -\epsilon k_{Af} P_1^s(N-1) & -\epsilon k_{Af} P_1^s(N-1) \\ -\epsilon k_{Af} P_1^s(N) & \dots & -\epsilon k_{Af} P_1^s(N) & -\epsilon k_{Af} P_1^s(N) & -k_{Ab}\alpha^N - \epsilon k_{Af} P_1^s(N) & -\epsilon k_{Af} P_1^s(N) \end{array} \right) \quad (\text{S3.6})$$

$$W_{32} = \left(\begin{array}{ccc|ccc} -\epsilon_{seq} k_{Af} P_1^s(0) & -\epsilon_{seq} k_{Af} P_1^s(0) & -\epsilon_{seq} k_{Af} P_1^s(0) & \dots & \dots & -\epsilon_{seq} k_{Af} P_1^s(0) \\ -\epsilon_{seq} k_{Af} P_1^s(1) & -\epsilon_{seq} k_{Af} P_1^s(1) & -\epsilon_{seq} k_{Af} P_1^s(1) & \dots & \dots & -\epsilon_{seq} k_{Af} P_1^s(1) \\ \vdots & \dots & \ddots & \dots & \dots & \vdots \\ -\epsilon_{seq} k_{Af} P_1^s(N-1) & \dots & -\epsilon_{seq} k_{Af} P_1^s(N-1) & -\epsilon_{seq} k_{Af} P_1^s(N-1) & -\epsilon_{seq} k_{Af} P_1^s(N-1) & -\epsilon_{seq} k_{Af} P_1^s(N-1) \\ -\epsilon_{seq} k_{Af} P_1^s(N) & \dots & -\epsilon_{seq} k_{Af} P_1^s(N) & -\epsilon_{seq} k_{Af} P_1^s(N) & -\epsilon_{seq} k_{Af} P_1^s(N) & -\epsilon_{seq} k_{Af} P_1^s(N) \end{array} \right) \quad (\text{S3.7})$$

To make things simpler let us look at just the \mathbf{W}' matrix elements,

$$\mathbf{W}' = \left(\begin{array}{c|c|c} W'_{11} & W'_{12} & W'_{13} \\ \hline W'_{21} & W'_{22} & W'_{23} \\ \hline W'_{31} & W'_{32} & W'_{33} \end{array} \right) \quad (\text{S3.8})$$

$$W'_{33} = \left(\begin{array}{ccc|ccc} -\epsilon k_{Af} P_1^s(0) & -\epsilon k_{Af} P_1^s(0) & \dots & -\epsilon k_{Af} P_1^s(0) \\ -\epsilon k_{Af} P_1^s(1) & -\epsilon k_{Af} P_1^s(1) & \dots & -\epsilon k_{Af} P_1^s(1) \\ \vdots & \dots & \ddots & \vdots \\ -\epsilon k_{Af} P_1^s(N) & \dots & -\epsilon k_{Af} P_1^s(N) & -\epsilon k_{Af} P_1^s(N) \end{array} \right) \quad (\text{S3.9})$$

$$W'_{32} = \left(\begin{array}{ccc|ccc} -\epsilon_{seq} k_{Af} P_1^s(0) & -\epsilon_{seq} k_{Af} P_1^s(0) & \dots & -\epsilon_{seq} k_{Af} P_1^s(0) \\ -\epsilon_{seq} k_{Af} P_1^s(1) & -\epsilon_{seq} k_{Af} P_1^s(1) & \dots & -\epsilon_{seq} k_{Af} P_1^s(1) \\ \vdots & \dots & \ddots & \vdots \\ -\epsilon_{seq} k_{Af} P_1^s(N) & \dots & -\epsilon_{seq} k_{Af} P_1^s(N) & -\epsilon_{seq} k_{Af} P_1^s(N) \end{array} \right) \quad (\text{S3.10})$$

Calculating the eigenvalues of W tells us about the stability of the steady state. Presence of +ve eigenvalues would indicate that the steady state is unstable and that a time-dependent steady state is present in the system. This would give rise to oscillations.

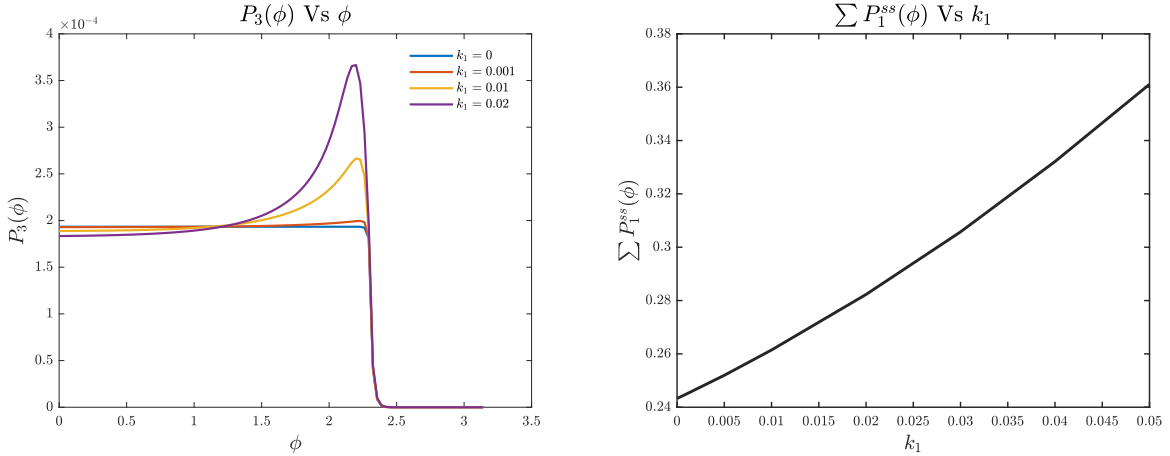
A. Origin of Instability

Increasing α leads to accumulation of probability density near the higher phosphorylated region of P_1 and P_3 states. Eventually, this leads to an instability. The oscillatory state is stable because higher α provides coherence to the wavepacket i.e. the phosphorylation wavepacket has a narrow width as it moves across the different states [21].

One simple way to understand the emergence of oscillations with increasing k_1 is through the Gershgorin circle theorem. The Gershgorin circle theorem provides us a way to estimate the location of the eigenvalues of any square matrix. Simply put, it says that for any square matrix W , if we construct the pair (W_{ii}, R_i) , where $R_i = \sum_{j, j \neq i} |W_{ji}|$, then all the eigenvalues of W lie in the union of circles with radii R_i and centred at W_{ii} . The onset of instability means the presence of +ve eigenvalues in the W matrix as mentioned before. In a normal rate matrix, all

the diagonal entries are -ve and the off-diagonal entries are +ve in a way such that sum of all element in each column is 0. Gershgorin theorem can be easily applied to this system and it can be seen that the eigenvalues will always have to be -ve (or 0). But in our case, the matrix W does have -ve off-diagonal elements, for instance $-\epsilon k_{Af} P_1^s(j) \eta_3(i), i \neq j$ term in the evolution of $\eta_3(j)$. All such terms which are -ve in the off-diagonal position have P_1^s . It is the presence of these terms which extend the Gershgorin circles into the positive half of the plane. So, our chances of obtaining a positive eigenvalue increases if we have higher $P_1^s(j) \forall j$. Now it remains to show that as K_{d0} increases, P_1^s either decreases or stays unchanged and when k_1 increases, P_1^s increases.

From (S2.33) we know the forms of the solution for $k_1 \neq 0$. For a moment let us take A_f to be fixed. This assumption is justified in the limit when k_1 is very small and there is not much change in the value of A_f derived in the $k_1 = 0$ case. For this fixed value of A_f let us consider two cases, the first when $k_1 = 0$ and the second when $k_1 \neq 0$. Fixed A_f implies that $\sum P_3(i) = \text{constant} = c$. Let us denote the functional form for $P_3(x)$ as $f(x)$ for case I and $g(x)$ for case II. As we have shown previously $f(x)$ is a constant function and $g(x)$ is a strictly increasing function. $\sum_x (f(x) - g(x)) = 0$ and the fact that $g(x)$ is strictly increasing implies that $f(x)$ and $g(x)$ have a single point where they cross each other i.e. $f(x) > g(x)$ for $x < x_c$, $f(x) = g(x)$ at $x = x_c$ and $f(x) < g(x)$ for $x > x_c$, where x_c is the point of crossover. Now $\sum_x (P_1^{II}(x) - P_1^I(x)) = \frac{K_{d0}}{A_f} \sum_x \alpha^x (g(x) - f(x))$. This is a polynomial in α with a single sign change in the coefficients at $x = x_c$, with 1 as a root and with the leading term $(g(x_N) - f(x_N))$ to be positive. Thus from Decartes rule for change in signs we can say that 1 is the only positive root of the polynomial and thus $\sum_x \alpha^x (g(x) - f(x)) > 0 \forall \alpha > 1$. Thus we can say that increasing k_1 increases $\sum_x P_1(x)$. This in turn affects the radii of the Gershgorin circles and thus the possibility of having an eigenvalue in the positive half of the complex plane increases with increasing k_1 .



(a) For $k_1 = 0$ we have a constant solution for $P_3(\phi)$. For $k_1 \neq 0$, we have a solution of the form (S2.34).

(b) This graph shows how the total probability in the P_1 form at steady state increases as a function of k_1 .

FIG. S6: Origin of Instability

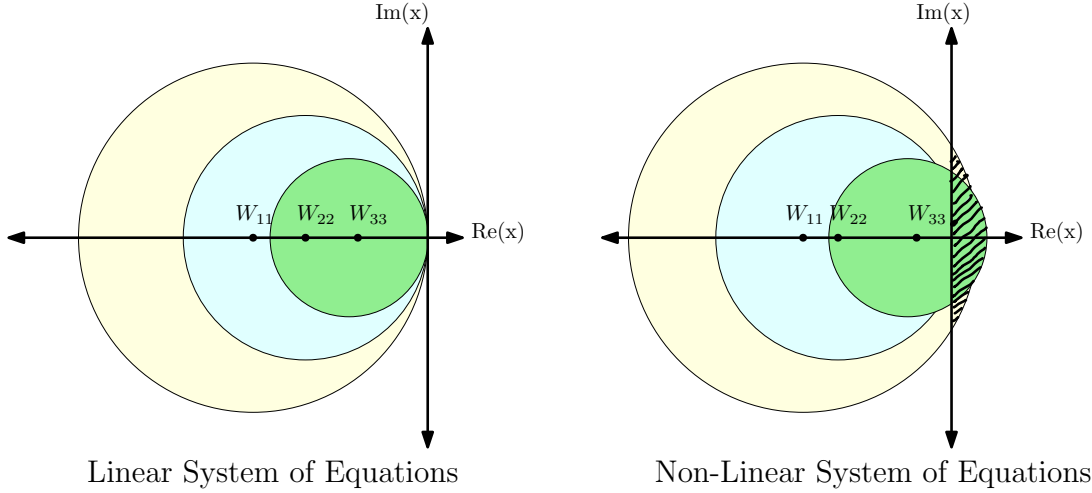


FIG. S7: All the eigenvalues lie in within the area of the union of all circles. In The linear case, the union of all circles lies completely in the left half of the Argand plane. Thus no eigenvalues are possible which have a +ve real part. In the nonlinear case, due to the -ve off diagonal terms, there is a possibility to have eigenvalues with +ve real part. If the shaded reagon has a greater area then chances of getting an instability increases.

S4. FIRST PASSAGE ANALYSIS

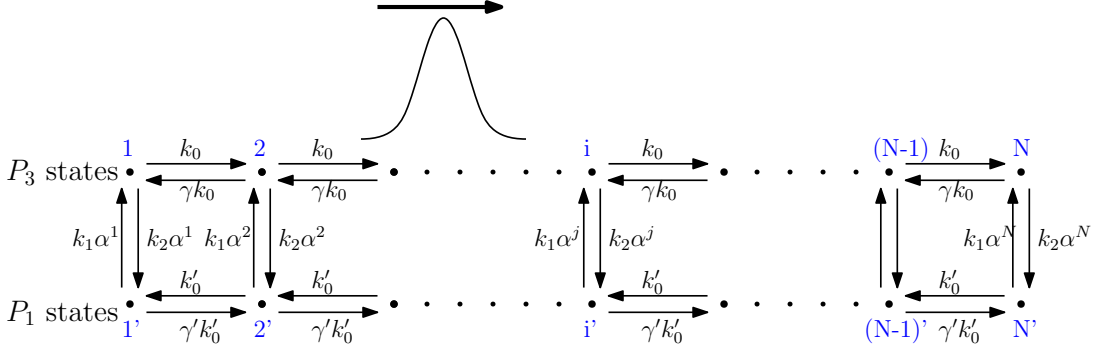


FIG. S8: The wave of phosphorylation moves across the P_1 and P_3 states. The movement of the wavepacket can be realized as a particle hopping between sites labelled with indices i (for P_3 states) and i' (for P_1 states)

In the notation used to solve the Fokker Planck equations, $k_1\alpha^x$ would correspond to $k_{A_f}A_f$, $k_2\alpha^x$ would correspond to $k_{A_{b0}}\alpha^{x-\pi}$, k_0' to k_1 and γ_0' to γ_1 . It is observed as the wavepacket moves, the free KaiA concentration changes with time as a function of α as, $A_f = A_{f0}\alpha^x$ where x is the position of the tip of the wavepacket.

Let T_n denote the time taken for the particle to reach the end for the first time, starting from the n^{th} position.

$$T_1 = \frac{k_2\alpha}{k_2\alpha + k_0} \left(T_{1'} + \frac{1}{k_2\alpha} \right) + \frac{k_0}{k_0 + k_2\alpha} \left(T_2 + \frac{1}{k_0} \right) \quad (S4.1)$$

$$T_{1'} = \frac{k_1\alpha}{k_1\alpha + \gamma_0'k_0'} \left(T_1 + \frac{1}{k_1\alpha} \right) + \frac{\gamma_0'k_0'}{k_1\alpha + \gamma_0'k_0'} \left(T_{2'} + \frac{1}{\gamma_0'k_0'} \right) \quad (S4.2)$$

$$T_2 = \frac{k_2\alpha^2}{k_0(1+\gamma) + k_2\alpha^2} \left(T_{2'} + \frac{1}{k_2\alpha^2} \right) + \frac{k_0}{k_0(1+\gamma) + k_2\alpha^2} \left(T_3 + \frac{1}{k_0} \right) + \frac{\gamma k_0}{k_0(1+\gamma) + k_2\alpha^2} \left(T_1 + \frac{1}{\gamma k_0} \right) \quad (S4.3)$$

$$T_{2'} = \frac{k_1\alpha^2}{k_0'(1+\gamma') + k_1\alpha^2} \left(T_2 + \frac{1}{k_1\alpha^2} \right) + \frac{\gamma_0'k_0'}{k_0'(1+\gamma') + k_1\alpha^2} \left(T_{3'} + \frac{1}{\gamma_0'k_0'} \right) + \frac{k_0'}{k_0'(1+\gamma') + k_1\alpha^2} \left(T_{1'} + \frac{1}{k_0'} \right) \quad (S4.4)$$

and so on and so forth. Define:

$$s_j = k_0(1+\gamma) + k_2\alpha^j \quad p_j = \frac{k_2\alpha^j}{s_j} \quad q_j = \frac{k_0}{s_j} \quad r_j = \frac{\gamma k_0}{s_j} \quad (S4.5)$$

and similarly for the indices j' . Using these definitions, we have,

$$T_j = p_j T_{j'} + q_j T_{j+1} + r_j T_{j-1} + 3s_j^{-1} \quad (\text{S4.6})$$

$$T_{j'} = p_{j'} T_j + r_{j'} T_{j'+1} + q_{j'} T_{j'-1} + 3s_{j'}^{-1} \quad (\text{S4.7})$$

$$\implies T_j = T_{j'} + \frac{3}{p_j s_j} + \frac{q_j - r_j}{p_j} \frac{\partial T_j}{\partial j} \quad (\text{S4.8})$$

$$T_{j'} = T_j + \frac{3}{p_{j'} s_{j'}} + \frac{r_{j'} - q_{j'}}{p_{j'}} \frac{\partial T_{j'}}{\partial j'} \quad (\text{S4.9})$$

Eliminating T' and relabelling j by x , we get,

$$\frac{(1-\gamma)(1-\gamma')k_0 k'_0}{k_1 k_2 \alpha^x} \frac{\partial^2 T}{\partial x^2} + \left[\frac{(1-\gamma)k_0}{k_2} - \frac{(1-\gamma')k'_0}{k_1} \right] \frac{\partial T}{\partial x} + 3 \left[\frac{1}{k_1} + \frac{1}{k_2} - \frac{(1-\gamma')k'_0 \ln \alpha}{k_1 k_2 \alpha^x} \right] = 0 \quad (\text{S4.10})$$

Assuming that T is linear in x for small k'_0 , the first term can be neglected. The solution of $T(x)$ is given as,

$$AT(x) = -\frac{C}{\ln \alpha} (1 - \alpha^{-L}) - B(x - L) \quad (\text{S4.11})$$

$$(\text{S4.12})$$

where, $A = \frac{(1-\gamma)k_0}{k_2} - \frac{(1-\gamma')k'_0}{k_1}$, $B = \frac{1}{k_1} + \frac{1}{k_2}$ and $C = \frac{(1-\gamma')k'_0 \ln \alpha}{k_1 k_2}$. The velocity of the wave packet is given by, $v = \frac{L}{T(0)}$. Putting in all the values, we get,

$$v = \frac{1}{3} \frac{(1-\gamma)k_0 - \frac{k_2}{k_1}(1-\gamma')k'_0}{1 + \frac{k_2}{k_1} - \frac{k'_0}{k_1}(1-\gamma') \ln \alpha} \approx \frac{1}{3} \frac{(1-\gamma)k_0 - \frac{k_2}{k_1}(1-\gamma')k'_0}{1 + \frac{k_2}{k_1}} \quad (\text{S4.13})$$

In the regime where we have oscillations, $k'_0 \ll k_1$. Thus the second term in the denominator can be ignored. We have, $\frac{k_2}{k_1} = \frac{k_{Ab0} \alpha^{-\pi}}{k_{Af} A_{f0}} = \frac{K_{d0}}{\alpha^\pi A_{f0}}$. This expression shows that with increase in K_{d0} , the velocity of the wavepacket decreases.

S5. PARAMETERS

k_0	2.5	γ	0.5	ω	10^{-1}
k_1	$0 \cdot 10^{-2}$	γ_1	10^{-2}	K_d	10^{-1}
k_{dp}	$2 \cdot 10^{-1}$	γ_{dp}	$5 \cdot 10^{-2}$	ω_1	1
$k_{Ab,0}$	10^3	K_{d0}	1-11	K_{d1}	10^{-1}
α	10	A_t	0.1	ϵ_{seq}	0

TABLE S1: Parameter Values for comparing Analytical prediction and Numerical Simulation in the $k_1 = 0$ case, i.e. when ultrasensitivity is absent.

k_0	2.5	γ	0.08	ω	10^{-1}
k_1	$1 \cdot 5 \cdot 10^{-2}$	γ_1	10^{-2}	K_d	10^{-2}
k_{dp}	$5 \cdot 10^{-2}$	γ_{dp}	$5 \cdot 10^{-2}$	ω_1	10^{-2}
$k_{Ab,0}$	10^3	K_{d0}	1-11	K_{d1}	10^{-2}
α	10	A_t	0.1	ϵ_{seq}	0.1

TABLE S2: Parameter Values for Numerical simulations in the $k_1 \neq 0$ case, i.e. when ultrasensitivity is present.

All numerical simulations were performed using ODE15s function of MATLAB. In all our simulations, the value of N was 100, i.e. there were 101 states of each type, P_1 , P_2 and P_3 .